



**IJOER**  
RESEARCH JOURNAL

# International Journal of Engineering Research & Science

ISSN  
2395-6992

[www.ijoer.com](http://www.ijoer.com)  
[www.adpublications.org](http://www.adpublications.org)

Volume-4! Issue-8! August, 2018 [www.ijoer.com](http://www.ijoer.com) ! [info@ijoer.com](mailto:info@ijoer.com)

## Preface

We would like to present, with great pleasure, the inaugural volume-4, Issue-8, August 2018, of a scholarly journal, *International Journal of Engineering Research & Science*. This journal is part of the AD Publications series *in the field of Engineering, Mathematics, Physics, Chemistry and science Research Development*, and is devoted to the gamut of Engineering and Science issues, from theoretical aspects to application-dependent studies and the validation of emerging technologies.

This journal was envisioned and founded to represent the growing needs of Engineering and Science as an emerging and increasingly vital field, now widely recognized as an integral part of scientific and technical investigations. Its mission is to become a voice of the Engineering and Science community, addressing researchers and practitioners in below areas

Chemical Engineering	
Biomolecular Engineering	Materials Engineering
Molecular Engineering	Process Engineering
Corrosion Engineering	
Civil Engineering	
Environmental Engineering	Geotechnical Engineering
Structural Engineering	Mining Engineering
Transport Engineering	Water resources Engineering
Electrical Engineering	
Power System Engineering	Optical Engineering
Mechanical Engineering	
Acoustical Engineering	Manufacturing Engineering
Optomechanical Engineering	Thermal Engineering
Power plant Engineering	Energy Engineering
Sports Engineering	Vehicle Engineering
Software Engineering	
Computer-aided Engineering	Cryptographic Engineering
Teletraffic Engineering	Web Engineering
System Engineering	
Mathematics	
Arithmetic	Algebra
Number theory	Field theory and polynomials
Analysis	Combinatorics
Geometry and topology	Topology
Probability and Statistics	Computational Science
Physical Science	Operational Research
Physics	
Nuclear and particle physics	Atomic, molecular, and optical physics
Condensed matter physics	Astrophysics
Applied Physics	Modern physics
Philosophy	Core theories

Chemistry	
Analytical chemistry	Biochemistry
Inorganic chemistry	Materials chemistry
Neurochemistry	Nuclear chemistry
Organic chemistry	Physical chemistry
Other Engineering Areas	
Aerospace Engineering	Agricultural Engineering
Applied Engineering	Biomedical Engineering
Biological Engineering	Building services Engineering
Energy Engineering	Railway Engineering
Industrial Engineering	Mechatronics Engineering
Management Engineering	Military Engineering
Petroleum Engineering	Nuclear Engineering
Textile Engineering	Nano Engineering
Algorithm and Computational Complexity	Artificial Intelligence
Electronics & Communication Engineering	Image Processing
Information Retrieval	Low Power VLSI Design
Neural Networks	Plastic Engineering

Each article in this issue provides an example of a concrete industrial application or a case study of the presented methodology to amplify the impact of the contribution. We are very thankful to everybody within that community who supported the idea of creating a new Research with IJOER. We are certain that this issue will be followed by many others, reporting new developments in the Engineering and Science field. This issue would not have been possible without the great support of the Reviewer, Editorial Board members and also with our Advisory Board Members, and we would like to express our sincere thanks to all of them. We would also like to express our gratitude to the editorial staff of AD Publications, who supported us at every stage of the project. It is our hope that this fine collection of articles will be a valuable resource for *IJOER* readers and will stimulate further research into the vibrant area of Engineering and Science Research.



Mukesh Arora  
(Chief Editor)

## **Board Members**

### **Mukesh Arora(Editor-in-Chief)**

BE(Electronics & Communication), M.Tech(Digital Communication), currently serving as Assistant Professor in the Department of ECE.

### **Dr. Omar Abed Elkareem Abu Arqub**

Department of Mathematics, Faculty of Science, Al Balqa Applied University, Salt Campus, Salt, Jordan, He received PhD and Msc. in Applied Mathematics, The University of Jordan, Jordan.

### **Dr. AKPOJARO Jackson**

Associate Professor/HOD, Department of Mathematical and Physical Sciences, Samuel Adegboyega University, Ogwa, Edo State.

### **Dr. Ajoy Chakraborty**

Ph.D.(IIT Kharagpur) working as Professor in the department of Electronics & Electrical Communication Engineering in IIT Kharagpur since 1977.

### **Dr. Ukar W.Soelistijo**

Ph D , Mineral and Energy Resource Economics, West Virginia State University, USA, 1984, Retired from the post of Senior Researcher, Mineral and Coal Technology R&D Center, Agency for Energy and Mineral Research, Ministry of Energy and Mineral Resources, Indonesia.

### **Dr. Heba Mahmoud Mohamed Afify**

h.D degree of philosophy in Biomedical Engineering, Cairo University, Egypt worked as Assistant Professor at MTI University.

### **Dr. Aurora Angela Pisano**

Ph.D. in Civil Engineering, Currently Serving as Associate Professor of Solid and Structural Mechanics (scientific discipline area nationally denoted as ICAR/08—"Scienza delle Costruzioni"), University Mediterranea of Reggio Calabria, Italy.

### **Dr. Faizullah Mahar**

Associate Professor in Department of Electrical Engineering, Balochistan University Engineering & Technology Khuzdar. He is PhD (Electronic Engineering) from IQRA University, Defense View, Karachi, Pakistan.

### **Dr. S. Kannadhasan**

Ph.D (Smart Antennas), M.E (Communication Systems), M.B.A (Human Resources).

### **Dr. Christo Ananth**

Ph.D. Co-operative Networks, M.E. Applied Electronics, B.E Electronics & Communication Engineering Working as Associate Professor, Lecturer and Faculty Advisor/ Department of Electronics & Communication Engineering in Francis Xavier Engineering College, Tirunelveli.

## **Dr. S.R.Boselin Prabhu**

Ph.D, Wireless Sensor Networks, M.E. Network Engineering, Excellent Professional Achievement Award Winner from Society of Professional Engineers Biography Included in Marquis Who's Who in the World (Academic Year 2015 and 2016). Currently Serving as Assistant Professor in the department of ECE in SVS College of Engineering, Coimbatore.

## **Dr. Maheshwar Shrestha**

Postdoctoral Research Fellow in DEPT. OF ELE ENGG & COMP SCI, SDSU, Brookings, SD  
Ph.D, M.Sc. in Electrical Engineering from SOUTH DAKOTA STATE UNIVERSITY, Brookings, SD.

## **Zairi Ismael Rizman**

Senior Lecturer, Faculty of Electrical Engineering, Universiti Teknologi MARA (UiTM) (Terengganu) Malaysia  
Master (Science) in Microelectronics (2005), Universiti Kebangsaan Malaysia (UKM), Malaysia. Bachelor (Hons.) and Diploma in Electrical Engineering (Communication) (2002), UiTM Shah Alam, Malaysia

## **Dr. D. Amaranatha Reddy**

Ph.D.(Postdoctoral Fellow,Pusan National University, South Korea), M.Sc., B.Sc. : Physics.

## **Dr. Dibya Prakash Rai**

Post Doctoral Fellow (PDF), M.Sc.,B.Sc., Working as Assistant Professor in Department of Physics in Pachhungga University College, Mizoram, India.

## **Dr. Pankaj Kumar Pal**

Ph.D R/S, ECE Deptt., IIT-Roorkee.

## **Dr. P. Thangam**

BE(Computer Hardware & Software), ME(CSE), PhD in Information & Communication Engineering, currently serving as Associate Professor in the Department of Computer Science and Engineering of Coimbatore Institute of Engineering and Technology.

## **Dr. Pradeep K. Sharma**

PhD., M.Phil, M.Sc, B.Sc, in Physics, MBA in System Management, Presently working as Provost and Associate Professor & Head of Department for Physics in University of Engineering & Management, Jaipur.

## **Dr. R. Devi Priya**

Ph.D (CSE),Anna University Chennai in 2013, M.E, B.E (CSE) from Kongu Engineering College, currently working in the Department of Computer Science and Engineering in Kongu Engineering College, Tamil Nadu, India.

## **Dr. Sandeep**

Post-doctoral fellow, Principal Investigator, Young Scientist Scheme Project (DST-SERB), Department of Physics, Mizoram University, Aizawl Mizoram, India- 796001.

## **Mr. Abilash**

MTech in VLSI, BTech in Electronics & Telecommunication engineering through A.M.I.E.T.E from Central Electronics Engineering Research Institute (C.E.E.R.I) Pilani, Industrial Electronics from ATI-EPI Hyderabad, IEEE course in Mechatronics, CSHAM from Birla Institute Of Professional Studies.

## **Mr. Varun Shukla**



M.Tech in ECE from RGPV (Awarded with silver Medal By President of India), Assistant Professor, Dept. of ECE, PSIT, Kanpur.

## **Mr. Shrikant Harle**

Presently working as a Assistant Professor in Civil Engineering field of Prof. Ram Meghe College of Engineering and Management, Amravati. He was Senior Design Engineer (Larsen & Toubro Limited, India).

## Table of Contents

S.No	Title	Page No.
1	<p><b>A multi-grid finite-volume method for free-surface flows</b>  <b>Authors:</b> Evangelia D. Farsirotou, Johannes V. Soulis</p> <p> <b>DOI:</b> 10.5281/zenodo.1407395</p> <p> <b>DIN Digital Identification Number:</b> IJOER-AUG-2018-1</p>	01-13
2	<p><b>New Formula for Lasik Surgery on Myopic &amp; Hypermetropic Eyes</b>  <b>Authors:</b> Prof.(Dr.) Bijay Kumar Parida, Ms.Anannya Anupurva</p> <p> <b>DOI:</b> 10.5281/zenodo.1407397</p> <p> <b>DIN Digital Identification Number:</b> IJOER-AUG-2018-2</p>	14-17
3	<p><b>Reducing the Amount of Hard Drive Memory Used For Storing Elements of Abstract Data Types</b>  <b>Authors:</b> Grigoriy Pronin, Olga Popova</p> <p> <b>DOI:</b> 10.5281/zenodo.1407399</p> <p> <b>DIN Digital Identification Number:</b> IJOER-AUG-2018-8</p>	18-22
4	<p><b>New Formula to Calculate the Size of the Corneal Flap for Autologous Ipsilateral Rotational Keratoplasty</b>  <b>Authors:</b> Prof.(Dr.) Bijay Kumar Parida, Ms.Anannya Anupurva</p> <p> <b>DOI:</b> 10.5281/zenodo.1407401</p> <p> <b>DIN Digital Identification Number:</b> IJOER-AUG-2018-9</p>	23-26
5	<p><b>Value-at-Risk of JCP Stock and Analysis of Calendar Effects</b>  <b>Authors:</b> Xinyan Zhang, Rong Zhang</p> <p> <b>DOI:</b> 10.5281/zenodo.1407403</p> <p> <b>DIN Digital Identification Number:</b> IJOER-AUG-2018-10</p>	27-37

6	<p><b>Biological Removal of Nitrogen and Phosphorus using Activated Sludge Treatment in Meat Processing Wastewaters</b></p> <p><b>Authors:</b> Anisa Myrtaj (Rexhepi), Acad. Assoc. Ilirjan Malollari</p> <p> <b>DOI:</b> 10.5281/zenodo.1407405</p> <p> <b>DIN Digital Identification Number:</b> IJOER-AUG-2018-12</p>	38-41
---	--	-------



# A multi-grid finite-volume method for free-surface flows

Evangelia D. Farsirotou<sup>1</sup>, Johannes V. Soulis<sup>2</sup>

<sup>1</sup>Department of Civil Engineering T.E., Faculty of Applied Sciences, Technological Educational Institute of Thessaly, 411 10 Larissa, Greece.

<sup>2</sup>Department of Civil Engineering, Fluid Mechanics/Hydraulics Division, Democritus University of Thrace, Xanthi 67100, Greece.

**Abstract**—A depth-averaged subcritical and/or supercritical, steady, free-surface flow numerical model is developed to calculate physical hydraulic flow parameters in open channels. The vertically averaged free-surface flow equations are numerically solved using an explicit finite-volume numerical scheme in integral form. The grid used may be irregular and conforms to the physical boundaries of any problem. A multi-grid algorithm has been developed and has subsequently been applied to accelerate the convergence solution. A grid clustering technique is also applied. The numerical approach is straight forward and the flow boundary conditions are easy enforced. The capabilities of the proposed method are demonstrated by analyzing subcritical flow in an abrupt converging-diverging open channel flume as well calculating supercritical flows in an expansion channel. The computed results are satisfactorily compared with available measurements as well as with other numerical technique results. Very coarse grid gives satisfactory comparison results. The explicit numerical code can be utilized, within the assumptions made about the nature of the flow, for various vertically averaged free-surface flow calculations. Scope is to simulate free-surface flows of practical interest in a straight forward way. It can be extended to channel designs.

**Keywords**—Multi-grid, Finite-volume, Subcritical-supercritical free-surface flow.

## I. INTRODUCTION

In recent years significant advances have been made in computational fluid dynamics applied to free-surface flow calculations. The flow pattern of the aforementioned open channels either natural or technical is highly complex. There exist classes of free-surface flow problems, which can adequately be described in the context of depth-averaged 2D mathematical models. These simplified representations of 3D flows are justified where turbulent mixing, due to bottom roughness, effectively generates a uniform velocity distribution over the depth of the flow field. For free-surface flows in complex geometry it is convenient to make predictions using non-orthogonal boundary fitted computational meshes.

Numerous publications were reported for 2D free-surface flow simulation, among them Soulis J. [16] developed an explicit finite-volume numerical technique, with transformed grid, to simulate subcritical and supercritical depth-averaged free-surface flows. Molls T. et al. [8] derived a depth-averaged open channel flow model while Molls T. et al [9] applied an alternative direction implicit scheme and the MacCormack explicit scheme, both second order accurate, to numerically simulate 2D flows near spur-dikes. Yulistiyanto B. et al [19] solved the continuity and momentum equations for 2D horizontal flow by vertical depth-integration and the differential equations were also evaluated using the MacCormack scheme. Lien H. et al [6] presented a 2D depth-averaged model for simulating flow pattern in channel bends using an orthogonal curvilinear coordinate system to efficiently simulate the flow field with irregular boundaries. The two-step split-operator approach consisting of the dispersion step and the propagation step with the staggered grid was used to numerically solve the flow governing equations. Molls T. et al [10] numerically simulated supercritical flow in a channel with a wavy sidewall by solving the 2D depth-averaged equations using two different second-order accurate finite-difference schemes, an implicit model that uses an alternating direction implicit technique to solve the governing equations and an explicit model employing the MacCormack two-step predictor-corrector scheme. Liu M. et al [7] presented an unsteady 2D depth-averaged flow model to simulate the bend-flow field by transforming the governing system of differential equations into an equivalent system applied over a square-grid network in order to overcome the difficulties and inaccuracies associated with the determination of characteristics near the flow boundaries. The MacCormack two-step explicit scheme with second-order accuracy was used for the solution of the transformed system of equations. Papanicolaou A. et al [11] performed a sensitivity analysis to examine the predictive capability of a 2D hydrodynamic model, a finite-element surface water modeling system to adequately describe the flow characteristics around emergent bendway weir structures. Chen Y. et al [1] presented the water stage prediction-correction method, based on the theory of characteristics to couple numerical models in the boundary-connected way for shallow-water flows. An 1D–2D coupled numerical model was established, which incorporates the artificial porosity method capable of treating wetting and drying. Yu C. et al [17] proposed a surface flow routing algorithm

based on numerical solutions of shallow water equations and the kinematic wave approximation. The shallow water equations were discretized by the first-order Godunov-type finite-volume method. An implicit dual time-stepping method was applied by Yu H. et al [18] to a Godunov-type finite-volume model for 2D shallow-water flows on unstructured grids to improve run-time efficiency. In this model, an implicit nonlinear lower-upper symmetric Gauss-Seidel solution algorithm was used as an inner iteration solver for the implicit dual time-stepping method. Hu D. et al [4] developed a 2D finite-volume Eulerian-Lagrangian method on unstructured grid for solving the advection equation in free-surface scalar transport models.

The current numerical model was developed by Farsirotou E. [2], at the Department of Civil Engineering in Aristotle University of Thessaloniki, Greece. A 2D, viscous flow, finite-volume computational algorithm has been developed. An efficient and reliable multiple-grid algorithm has been applied to accelerate the convergence solution. The corrections to the fine-grid points are transferred to a coarse grid to maintain the low truncation errors associated with fine level of discretizations. Dense grid is incorporated wherever high gradient regions are encountered. Viscous flow stresses are described using either fixed value eddy viscosity coefficient or values related to the flow properties. Purpose of this research was, a) to develop a simple and easy to program algorithm without grid transformation, b) to achieve fast convergence multi-grid algorithm requiring minimal programming and c) to apply very coarse grid in achieving satisfactory comparisons with measurements. Scope is to simulate free-surface flows of practical interest in a straight forward way.

## II. NUMERICAL MODEL

### 2.1 Theoretical assumptions

The channel flow is assumed to be homogeneous, incompressible and 2D with wind and Coriolis forces neglected. Hydrostatic pressure distribution is assumed throughout the flow field. The unsteady, free-surface flow in channels with fixed bed is described by non-linear, partial differential equations,

$$-\frac{\partial h}{\partial t} = \frac{\partial(hu)}{\partial x} + \frac{\partial(hv)}{\partial y} \quad (1)$$

$$-\frac{\partial(hu)}{\partial t} = \frac{\partial(gh^2/2 + hu^2)}{\partial x} + \frac{\partial(huv)}{\partial y} - gh(S_{ox} - S_{fx}) \quad (2)$$

$$-\frac{\partial(hv)}{\partial t} = \frac{\partial(gh^2/2 + hv^2)}{\partial y} + \frac{\partial(huv)}{\partial x} - gh(S_{oy} - S_{fy}) \quad (3)$$

x and y represent the Cartesian coordinate positions in the longitudinal and transverse directions respectively; t the time; u and v the average cross the depth velocity components in the x and y directions, respectively; h the water depth; g the gravity acceleration;  $S_{ox} = -\partial z_b / \partial x$  and  $S_{oy} = -\partial z_b / \partial y$  the channel slopes with  $z_b$  the bottom elevation above a datum and  $S_{fx}$  and  $S_{fy}$  the friction slopes defined, Kassem A. et al. [5], as,

$$S_{fx} = \frac{n^2 u \sqrt{u^2 + v^2}}{h^{4/3}} \text{ and } S_{fy} = \frac{n^2 v \sqrt{u^2 + v^2}}{h^{4/3}} \quad (4)$$

n is the Manning's flow friction coefficient. It is assumed that all of the resistance is due to bottom friction, thus neglecting the boundary layers on the side-walls, Molls T. et al. [8].

### 2.2 Application areas

Open channel flow problems, which can be adequately described in the context of depth-averaged, 2D mathematical models, where the flow properties can be assumed to be invariant along the vertical direction, are accurately simulated with the numerical model. The proposed program can be applied for free-surface determination in complex geometries with or without any obstructions into the flow region. Subcritical, supercritical or mixed subcritical-supercritical flows with automatic capturing of hydraulic jumps can also be simulated. In particular, the numerical code can be utilized for the calculation of:

- uniform flow using various flow friction coefficients,

- gradually varied flow as transitions, non-prismatic channels, backwater effects of dams etc,
- rapidly varied flow as parts of flow over spillways, hydraulic jumps in sloping channels, stilling basins, etc.

The code can be extended to, unsteady flows, morphology problems and channel designs.

### III. NUMERICAL SIMULATION

#### 3.1 Flow discretization

This program utilizes the finite-volume numerical method to solve the non-linear, parabolic, partial differential equations, Eqs. (1)-(3) in integral form, i.e. by applying the equations of continuity, x- and y-momentum to a series of finite-volumes with adjacent volumes sharing a common face, Farsirotou E. [2] and Soulis J. [16]. At the end of each time-step  $\Delta t$  the net flux into each elemental volume is zero, so that overall water mass flow is conserved, and the changes in momentum are equal to the forces imposed by the boundaries of the system. The 2D flow equations may be written down as conservation equations for a control volume  $\Delta V$  of unit height and for a time step  $\Delta t$  as,

$$-\Delta h = [\Delta(hu)\Delta y + \Delta(hv)\Delta x] \frac{\Delta t}{\Delta x \Delta y} \quad (5)$$

$$-\Delta(hu) = [\Delta(gh^2/2 + hu^2)\Delta y + \Delta(huv)\Delta x] \frac{\Delta t}{\Delta x \Delta y} - gh(S_{ox} - S_{fx})\Delta t \quad (6)$$

$$-\Delta(hv) = [\Delta(gh^2/2 + hv^2)\Delta x + \Delta(huv)\Delta y] \frac{\Delta t}{\Delta x \Delta y} - gh(S_{oy} - S_{fy})\Delta t \quad (7)$$

The physical domain i.e. flow region is divided into polygonal sub-areas with quadrilateral form. These sub-areas are called finite-volumes of unit depth. The governing flow equations are solved in a non-transformed grid (physical grid). The solution attributes values for water depth  $h$ , axial  $u$  and tangential  $v$  velocities at each grid node. Application results into a series of arithmetic equations with nodal values of water depth, axial and tangential velocities as equation unknowns. Figure 1 shows the notation used for mass-flux balancing across a flow finite-volume. Similar notation is adopted for the balancing of x- and y-momentum. For ease application, all  $\Delta y$ s are perpendicular to the x-axis. Thus, for water mass flux, an XFLUX is defined,

$$(XFLUX)_{i,j} = \left[ \frac{(hu)_{i+1,j} + (hu)_{i,j}}{2} \right] \Delta y \quad (8)$$

The YFLUX is defined,

$$(YFLUX)_{i,j} = \left[ \frac{(hv)_{i,j-1} + (hv)_{i,j}}{2} \right] \Delta x - \left[ \frac{(hu)_{i,j-1} + (hu)_{i,j}}{2} \right] \Delta y \quad (9)$$

The second term comes from the mass fluxes balance into the ABE flow region, Fig.1. The  $\Delta y$  term is also defined in Fig. 1. The terms  $\Delta(hu)$  and  $\Delta(hv)$  of Eq. (5) are defined:

$$\Delta(hu) = (XFLUX)_{i,j} - (XFLUX)_{i,j-1} \quad (10)$$

$$\Delta(hv) = (YFLUX)_{i+1,j} - (YFLUX)_{i,j} \quad (11)$$

Similar differences are applied to all  $\Delta$  terms, of Eqs. (6), (7). Thus, the water depth difference  $\Delta h$  in each  $i,j$  node of the involved finite-volume is calculated as,

$$\Delta h_{i,j} = \left[ (XFLUX)_{i,j} - (XFLUX)_{i,j-1} + (YFLUX)_{i+1,j} - (YFLUX)_{i,j} \right] \frac{\Delta t}{\Delta x \Delta y} \quad (12)$$

Similar calculations are performed for the x-and y-momentum flux balancing. Backward differencing is used for the  $\frac{\Delta}{\Delta x}$  estimation, while forward differencing is used for the  $\frac{\Delta}{\Delta y}$  estimation. The slopes  $S_{ox}$  and  $S_{oy}$  are pre-calculated and stored

at the beginning of each time step, while the friction slopes  $S_{fx}$  and  $S_{fy}$  are continuously updated. For all bed and friction slopes, averaged values of the appropriate physical quantities are used.

**3.2 Flow stabilization**

The changes  $\Delta h$ ,  $\Delta(hu)$  and  $\Delta(hv)$  are distributed between the four corners A, B, C and D of the finite-volume of Fig.1. However, this distribution affects the stability and the accuracy of the method. In the current research work it was decided to send 40.0% information regarding  $\Delta h$  change to the upstream face of the finite-volume, while the remaining 60.0% is sent to the downstream face. The  $\Delta(hu)$  and  $\Delta(hv)$  changes are taken as the averaged values of  $i$  and  $i-1$  nodes of the computational grid. Also, and this is crucial in achieving convergence, the water depth value  $h$  is calculated taking into account the currently involved finite-volume depth and the one located at immediate downstream. The decision was made after numerical experimentation. All changes  $\Delta h$ ,  $\Delta(hu)$  and  $\Delta(hv)$  were not directly used to yield the  $h$ ,  $hu$  and  $hv$  values. For all test runs a  $C_1$  factor is used for the  $h$  estimation and a  $C_2$  for the  $(hu)$  and  $(hv)$  calculations,

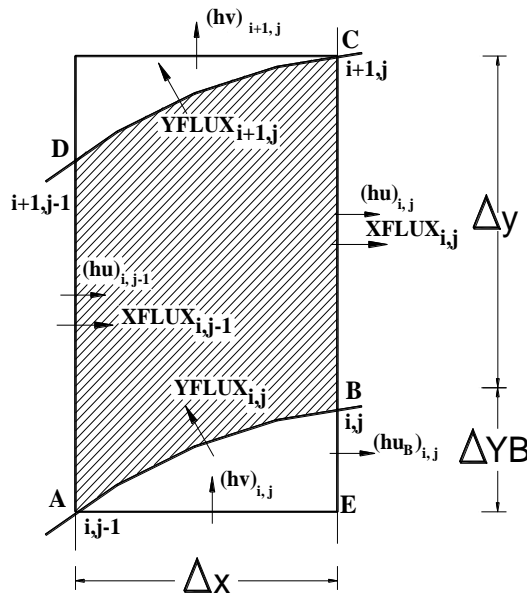


**FIG. 1. NOTATION FOR THE MASS FLUX ACROSS A FINITE-VOLUME**

$$h_{i,j}^{n+1} = h_{i,j}^n + \frac{\Delta h_{i,j}^{n+1}}{1 + \frac{C_1}{h_{1,1}^0} \Delta h_{i,j}^{n+1}} \tag{13}$$

$$(hu)_{i,j}^{n+1} = (hu)_{i,j}^n + \frac{\Delta(hu)_{i,j}^{n+1}}{1 + \frac{C_2}{(hu)_{1,1}^0} \Delta(hu)_{i,j}^{n+1}} \tag{14}$$

$n$  is the iteration number. Similar expression holds for  $(hv)$  calculation. The above empirical coefficients numerically derived with typical values  $C_1=0.1$  and  $C_2=0.025$  are needed to stabilize the solution particularly during at the first  $\Delta t$  time-steps. These empirical values have minimal influence on the solution convergence after the first time-steps. The numerical scheme was found to be stable over a wide range of  $C_1$  and  $C_2$  values.

**3.3 Multi-grid approach**

The multi-grid algorithm described here consists of a fine-grid solution procedure and a coarse-grid acceleration scheme, Soulis J. [14]. In the current approach, the solution is advanced simultaneously on coarse and on fine-grid. Figure 2 shows a  $2 \times 2$  multi-grid block. Thus, a coarse grid is formed grouping several finite-volumes into a block. The  $\Delta h$ ,  $\Delta(hu)$  and  $\Delta(hv)$ , changes, Eqs. (5)-(7), at the end of every time-step are known for each finite-volume of the fine-grid mesh. The

changes for the block can be found by summing the fluxes around its faces. Another way to find the changes for the block is to sum the already calculated changes for the finite-volume within the block.

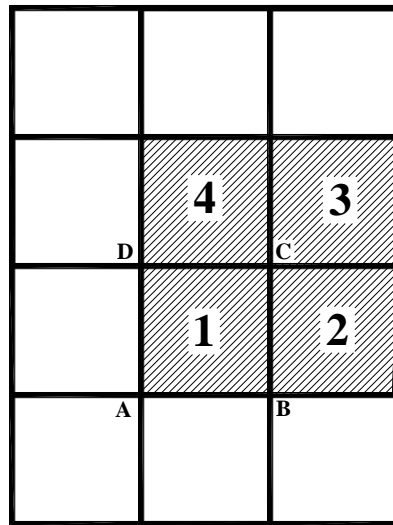


FIG. 2. A TYPICAL 2X2 MULTI-GRID

For a typical 2x2 block size application these changes are determined as follows,

$$\Delta h_{2 \times 2} = \Delta h_1 + \Delta h_2 + \Delta h_3 + \Delta h_4 \quad (15)$$

subscripts 1,2,3,4 denote the mesh control volumes, Fig. 2. Similarly,

$$\Delta(hu)_{2 \times 2} = \Delta(hu)_1 + \Delta(hu)_2 + \Delta(hu)_3 + \Delta(hu)_4 \quad (16)$$

$$\Delta(hv)_{2 \times 2} = \Delta(hv)_1 + \Delta(hv)_2 + \Delta(hv)_3 + \Delta(hv)_4 \quad (17)$$

Thereafter, the flow properties changes at fine-grid points are calculated,

$$\Delta h_1^{\text{new}} = \Delta h_1 + I_{2 \times 2}^{\text{fine}} \Delta h_{2 \times 2} \quad (18)$$

$$\Delta(hu)_1^{\text{new}} = \Delta(hu)_1 + I_{2 \times 2}^{\text{fine}} \Delta(hu)_{2 \times 2} \quad (19)$$

$$\Delta(hv)_1^{\text{new}} = \Delta(hv)_1 + I_{2 \times 2}^{\text{fine}} \Delta(hv)_{2 \times 2} \quad (20)$$

$I_{2 \times 2}^{\text{fine}}$  is a linear interpolation operator. The calculations using Eqs. (18)-(20) are repeated for the remaining 2, 3 and 4 finite-volumes of the under consideration block. With the multiple grid application, the use of the blocks minimizes the computational work needed to propagate the unsteady waves out of the computational domain so that a steady-state solution is rapidly reached. The convergence of the multi-grid method is typically 3 times faster than a single grid. Figure 3 shows the convergence histories for supercritical type of flow calculation using various multi-block schemes. The 2x2 multi-grid block give the fastest convergence for current method applications.

### 3.4 Grid clustering

Computational grid formation requires minimum data. Grid nodes need not to be uniform in any direction. Flow problems with large gradients of the physical quantities need dense computational grid formation for efficient flow depiction. Then, rather using a uniform grid distribution in the tangential direction grid points may be clustered in high flow gradients regions. This reduces the total amount of required grid points. For a physical domain enclosed by lower and upper solid surfaces (channel flow) clustering at both surfaces may be considered. The following algebraic equation may be employed for this purpose, Hoffman K. et al. [3],

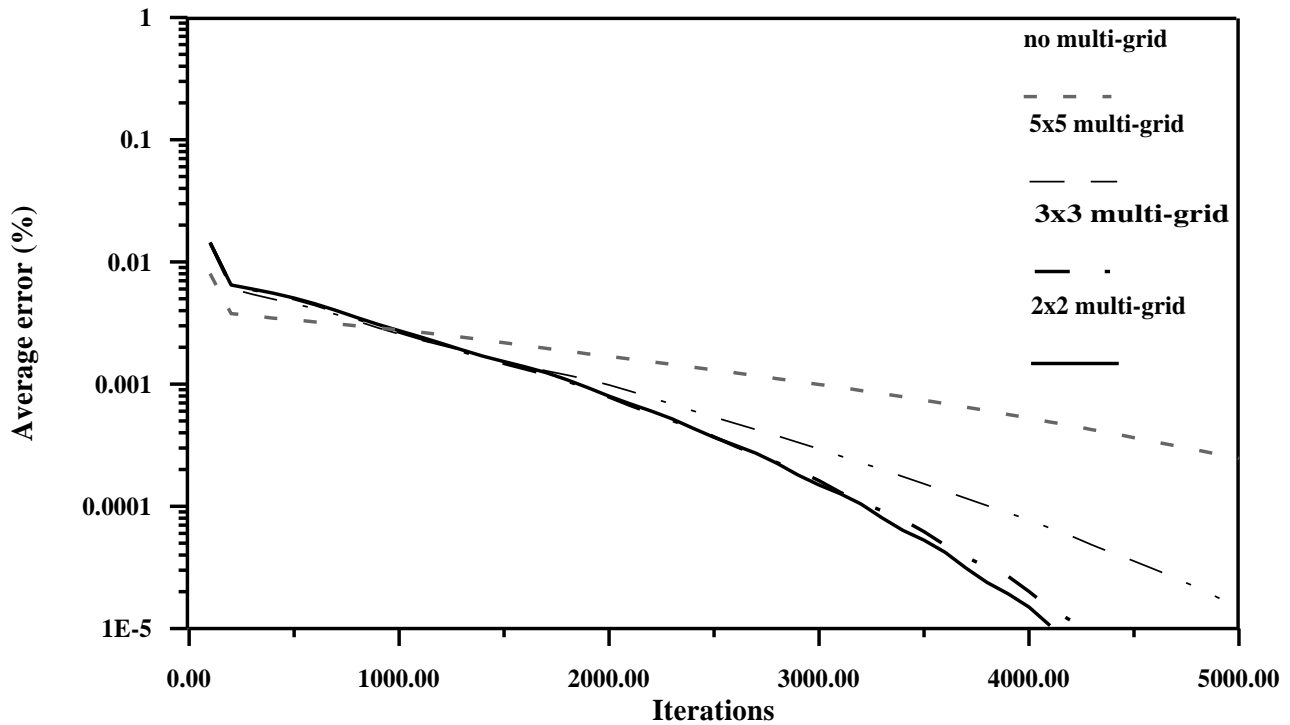


FIG. 3. CONVERGENCE HISTORY FOR THE ROUSE H. ET AL. (1951) EXPANSION CHANNEL USING VARIOUS MULTI-GRIDS

$$y(i, j) = y(1, j) + [y(IM, j) - y(1, j)] \frac{(2a + b)(BETA)^{ALFA} + 2a - b}{(2a + 1)(1 + BETA)^{ALFA}} \quad (21)$$

$$ALFA = \frac{i-1}{IM-1} - a, \quad BETA = \frac{b+1}{b-1} \quad (22)$$

IM is the maximum number of grid points in the transverse direction, b is a clustering parameter with values ranging from 1.05 for dense grid to 1.20 for less dense, while the factor a defines where the clustering takes place. Using a=0.0 clustering takes place at the upper wall while for a=0.5 clustering takes place at lower and upper wall.

### 3.5 Flow boundary conditions

There are two types of boundary conditions; the open boundaries and the solid boundaries. For subcritical flow entrance, at the upstream boundary a fixed value of the flow rate Q and a relative flow direction are specified. At the downstream boundary, a uniform across the width, water depth h is specified. For supercritical flow entrance, at the upstream boundary, the transverse flow velocity v component and a uniform across the width water depth h are specified along with total available head. At the downstream boundary all flow physical quantities left free to change. Simply, the physical quantity values are extrapolated from the interior grid nodes.

To close the problem, the condition of no water mass-flow across the solid boundaries needs to be applied (free-slip condition). This means that the velocity component normal to the solid face must be zero. This is easily achieved with the current grid formation and numerical discretization.

### 3.6 Numerical procedure

Firstly, geometrical and physical data describing the flow problem are read. Thereafter, the computational grid is formed. From the bed elevation the initial bottom slopes of the under examination channel are formed. A linear distribution of the  $gh^2/2$  quantity between inlet and outlet flow boundaries is assumed and the u, v velocity components, as well as the water depth h are calculated. The iterations start by solving the water mass-flux Eq. (5) to obtain  $h^{n+1}$ , using old  $u^n$ ,  $v^n$  and  $h^n$  and a corrected water depth is obtained. Then appropriate boundary flow conditions are applied at the inlet and outlet flow field.

Equations (6) and (7) are solved to obtain  $(hu)^{n+1}$  and  $(hv)^{n+1}$  and thereby new values for  $u^{n+1}$  and  $v^{n+1}$  are derived. Solid boundary conditions are applied requiring no water flow perpendicular to solid surface. Also, smoothing factors are applied to all changes of the flow field quantities. All changes are sent to the appropriate nodes of the finite-volume involved.

The convergence criterion requires that the averaged over the flow field relative error based on the axial velocity drops below  $5 \times 10^{-6}$ . As with all time-marching methods the theoretical maximum stable time step  $\Delta t$  is specified according to the Courant-Friedrichs-Lewy (CFL) criterion,

$$\Delta t \leq \left\{ \min \left( \frac{\Delta x}{u_{i,j} + \sqrt{gh_{i,j}}}, \frac{\Delta y}{v_{i,j} + \sqrt{gh_{i,j}}} \right) \right\} FT \quad (23)$$

$\Delta x (=x_{i,j}-x_{i,j-1})$  and  $\Delta y (=y_{i+1,j}-y_{i,j})$  are the streamwise and transverse distances of a given finite-volume, respectively. The actually used values are calculated using the minimum of all  $\Delta x$ s and  $\Delta y$ s of the grid. FT is a constant with less than unity value.

The described method is an explicit numerical technique requiring substantial computational time to achieve solution at the requested time level. The incorporation of the multi-grid approach ensures substantially faster convergence. The explicit formation is in favor of an implicit technique as far as the programming complexity is concerned. Programming the free-surface algorithm is straight forward process. The algorithm is written in a Fortran language.

#### IV. APPLICATIONS

##### 4.1 2D subcritical flow in a converging-diverging channel

The reliability of the current model in subcritical flows is confirmed by comparing numerical results with available measurements conducted by Soulis J. et al. [15]. Schematic plan view geometry of the tested laboratory flume (spur dike) is shown in Fig. 4. This flume was used to validate the numerical model simulation in subcritical free-surface flow. The channel length and width are 2.5 m and 0.25 m, respectively. At an axial, from inlet, distance 0.5 m the channel converges with a contraction angle of  $10.88^\circ$ . The convergence continues until the flume width reaches 0.125 m. The throat area extends 0.30 m. Thereafter, the lower side wall diverges with an expansion angle of  $21.037^\circ$  until the width takes the value of 0.25 m.

For the numerical simulation a  $48 \times 11$  (longitudinal x tangential) computational grid is used. The spatial step  $\Delta y$  is 0.025 m. However, the spatial step  $\Delta x$  for the converging part as well as for the throat region is 0.05 m while for the diverging part it is 0.025 m. The applied inflow discharge  $Q$  is  $0.02606 \text{ m}^3/\text{s}$ , while the downstream flow depth  $h$  is 0.284 m (subcritical flow conditions). The channel bottom slopes  $S_{0x}$  and  $S_{0y}$  are set zero. The Manning's flow friction coefficient  $n$  is estimated 0.012. Computational results of flow depth  $h$  and axial velocity magnitude  $u$  are presented along 3 different "streamlines". These are stream wise lines where measurements were taken at transverse distances of 0.05 m, 0.10 m and 0.20 m from the lower channel wall.

Comparisons between computed results and measurements, Soulis J. et al. [15], for the 0.05 "streamline" are shown in Fig. 5 for the water depth  $h$  and Fig. 6 for the  $u$  axial velocity magnitude. Axial velocities at the downstream end to the spur dike region were not available. Figures 7, 8, 9 and 10 show the water depth  $h$  and the axial velocity magnitude  $u$  for the 0.10 m and 0.20 m "streamlines" locations, respectively.

It is evident that the computed results agree rather well with the experimental measurements, particularly in the converging part of the channel. A discrepancy appears between measured and computed velocities in the diverging part of the channel, Fig. 10, where high viscous flow is developing. The tested spur dike obstacle constitutes a major difficulty from computational fluid dynamics point of view. Recirculating flow is present at the downstream spur dike end. However, the tested grid is sparse enough to adequately cover this highly turbulent region. The flow depths at the three "streamlines", both upstream and downstream from the converging part of the channel are also in good agreement with measurements and show the validity and practical reliability of the numerical model.

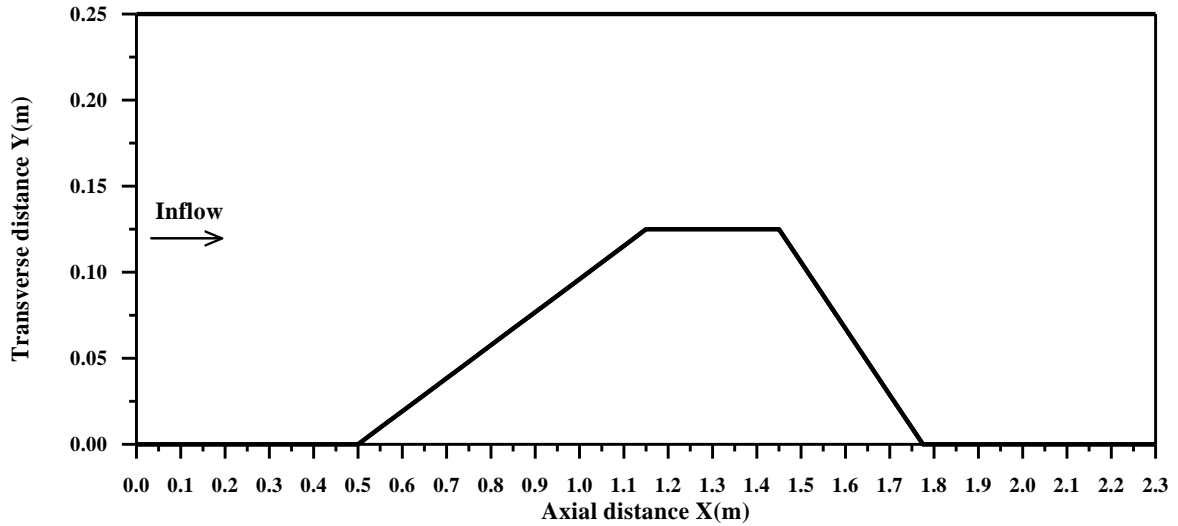


FIG. 4. CONVERGING- DIVERGING FLUME GEOMETRY

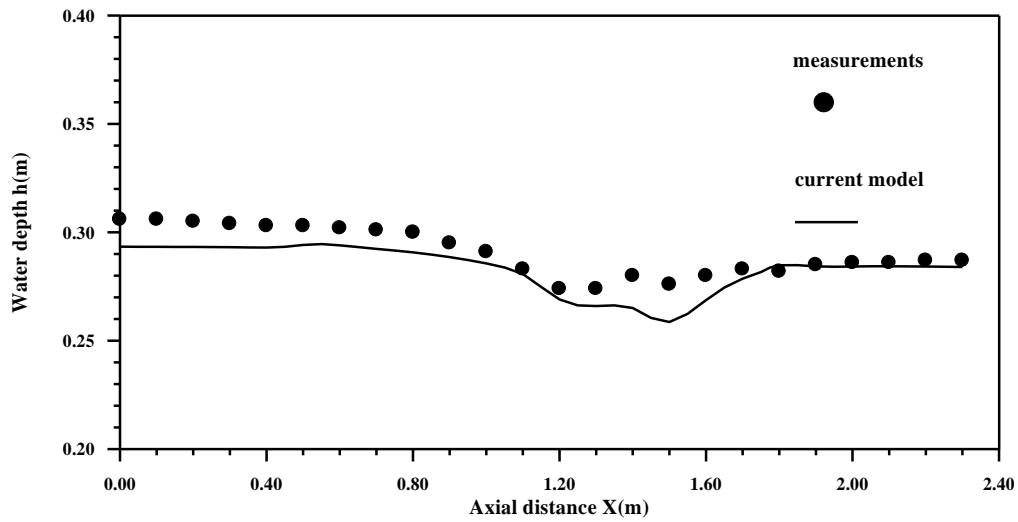


FIG. 5. WATER DEPTH COMPARISON BETWEEN CURRENT METHOD PREDICTIONS AND MEASUREMENTS ALONG A “STREAMLINE” LOCATED AT 0.05 M FROM LOWER WALL FOR THE CONVERGING-DIVERGING FLUME AT  $Q=0.02606 \text{ M}^3/\text{S}$

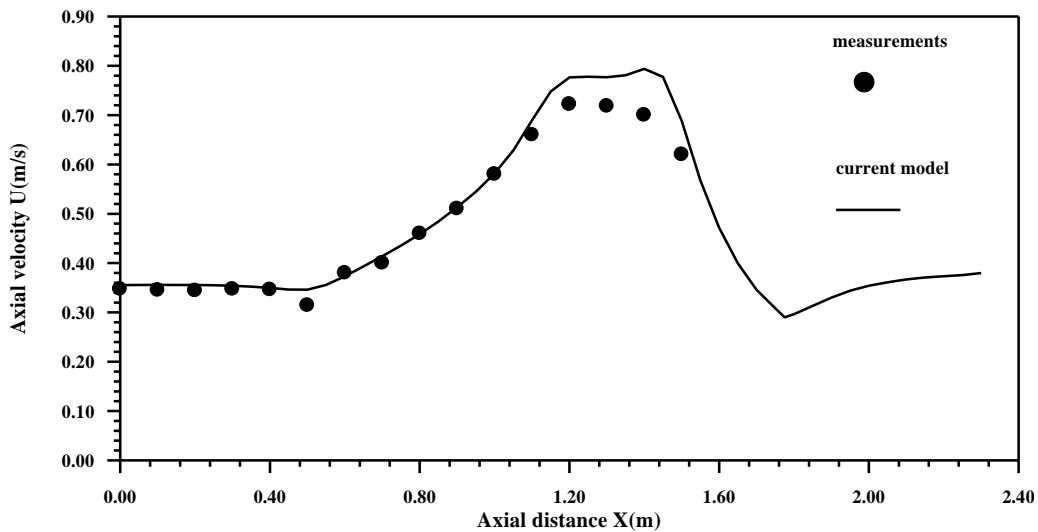
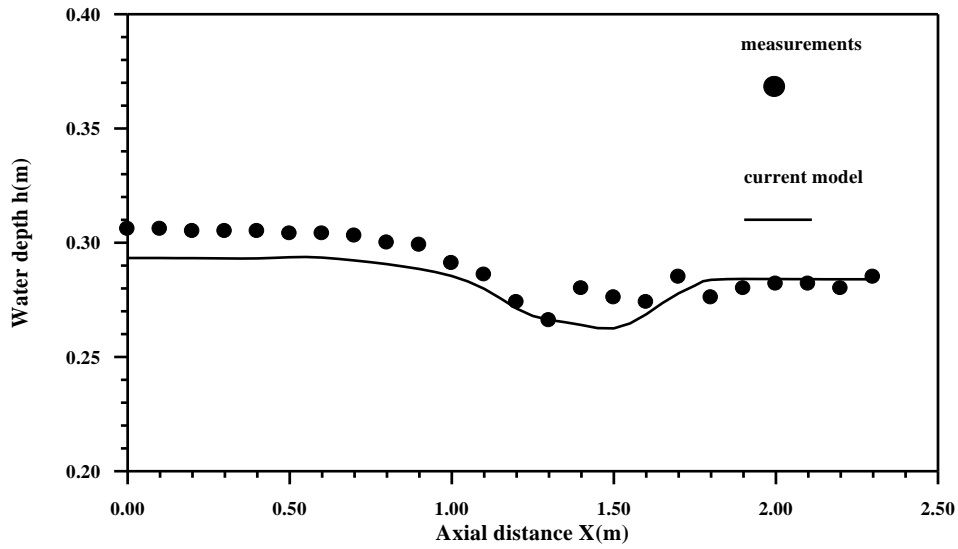
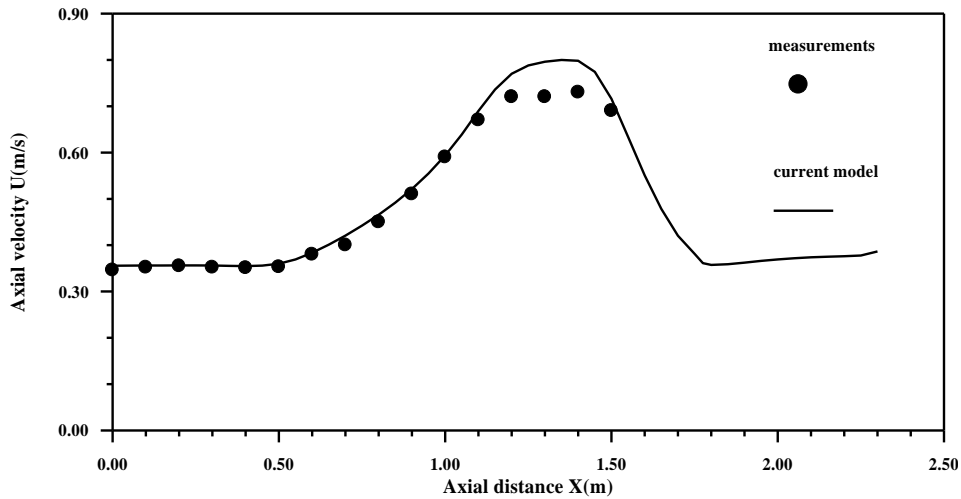


FIG. 6. AXIAL VELOCITY COMPARISON BETWEEN CURRENT METHOD PREDICTIONS AND MEASUREMENTS ALONG A “STREAMLINE” LOCATED AT 0.05 M FROM LOWER WALL FOR THE CONVERGING-DIVERGING FLUME AT  $Q=0.02606 \text{ M}^3/\text{S}$





**FIG.7. WATER DEPTH COMPARISON BETWEEN CURRENT METHOD PREDICTIONS AND MEASUREMENTS ALONG A “STREAMLINE” LOCATED AT 0.10 M FROM LOWER WALL FOR THE CONVERGING-DIVERGING FLUME AT  $Q=0.02606 \text{ M}^3/\text{S}$**



**FIG. 8. AXIAL VELOCITY COMPARISON BETWEEN CURRENT METHOD PREDICTIONS AND MEASUREMENTS ALONG A “STREAMLINE” LOCATED AT 0.10 M FROM LOWER WALL FOR THE CONVERGING-DIVERGING FLUME AT  $Q=0.02606 \text{ M}^3/\text{S}$**

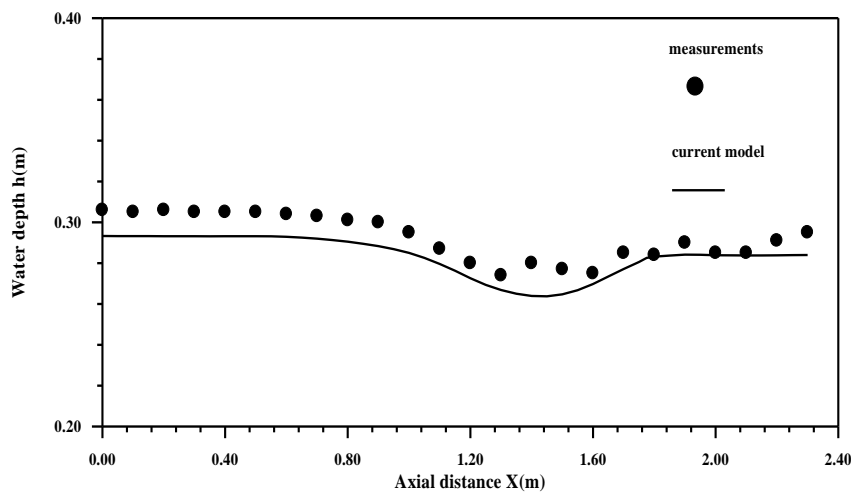


**FIG. 9. WATER DEPTH COMPARISON BETWEEN CURRENT METHOD PREDICTIONS AND MEASUREMENTS ALONG A “STREAMLINE” LOCATED AT 0.20 M FROM LOWER WALL FOR THE CONVERGING-DIVERGING FLUME AT  $Q=0.02606 \text{ M}^3/\text{S}$**

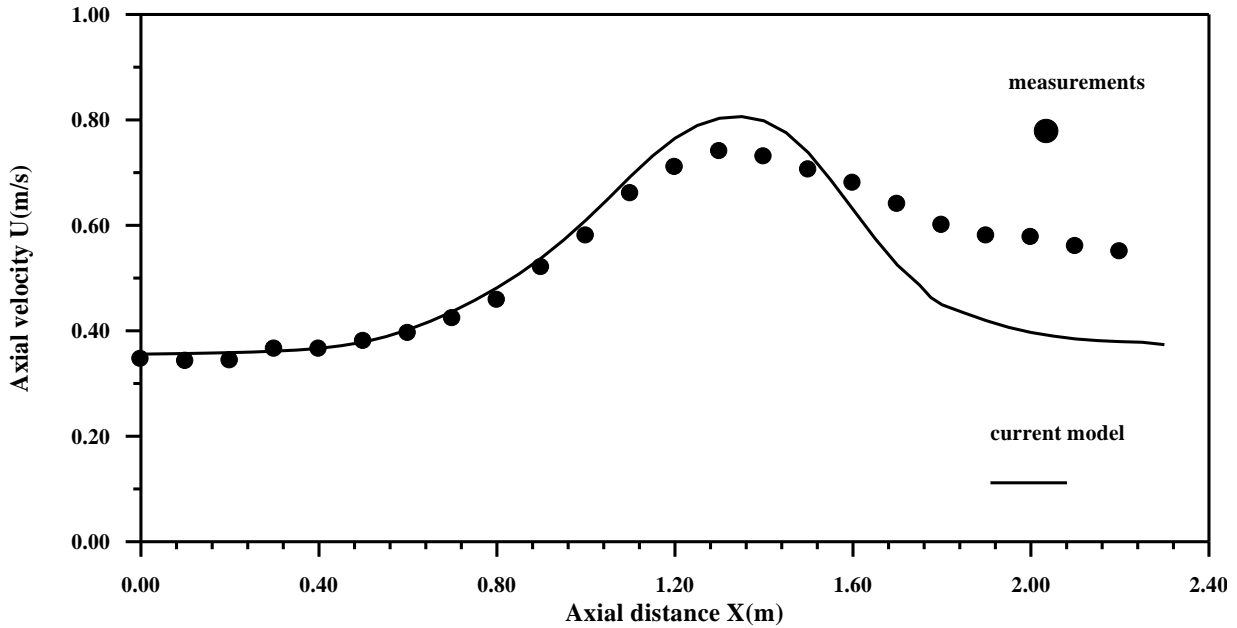


**FIG. 10. AXIAL VELOCITY COMPARISON BETWEEN CURRENT METHOD PREDICTIONS AND MEASUREMENTS ALONG A “STREAMLINE” LOCATED AT 0.20 M FROM LOWER WALL FOR THE CONVERGING-DIVERGING FLUME AT Q=0.02606 M<sup>3</sup>/S**

**4.2 2D supercritical flow in an expansion channel**

The channel expansion, shown in Fig. 11, is used to test the accuracy of the proposed numerical method at high entrance Froude number of  $Fr_1=4.0$ . Rouse H. et al. [12] experimentally studied supercritical flow for the channel expansion. A 61x29 grid node is used for numerical simulation. The actual expansion channel geometry is described as,

$$\frac{y}{b_1} = \frac{1}{2} \left( \frac{x}{4.0b_1} \right)^{3/2} + \frac{1}{2} \tag{24}$$

$b_1$  is the half entrance width. At the upstream end, a constant value of water depth  $h_1$  of 1.0 m is specified. A fixed value of the total available head 9.0 m is also specified. The Manning’s roughness coefficient is 0.012.

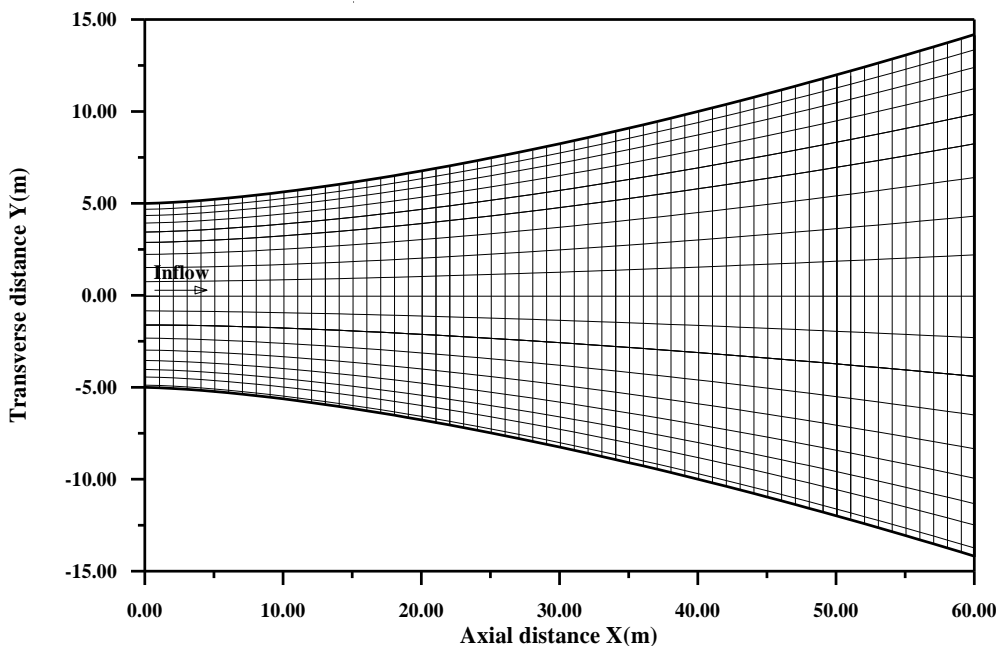


**FIG. 11. EXPANSION CHANNEL GEOMETRY FOR  $Fr_1=4.0$  AFTER ROUSE H. ET AL. (1951), CLUSTERED COMPUTATIONAL GRID**

The current method computational results are compared with measurements, Rouse H. et al. [12] as well as with computational results using an explicit MacCormack numerical scheme, Soulis J. et al. [13]. Figures 12, 13 and 14 show the comparison for the curved side, mid-stream line (line between axis of symmetry and curved side) and axis of symmetry, respectively. The current model comparison results with either measurements or with MacCormack's numerical method is considered to be satisfactory. It must be noted that the predicted results are closer to each other. The overall performance demonstrates that the proposed model is accurate and efficient for simulating free-surface flow in practical applications.

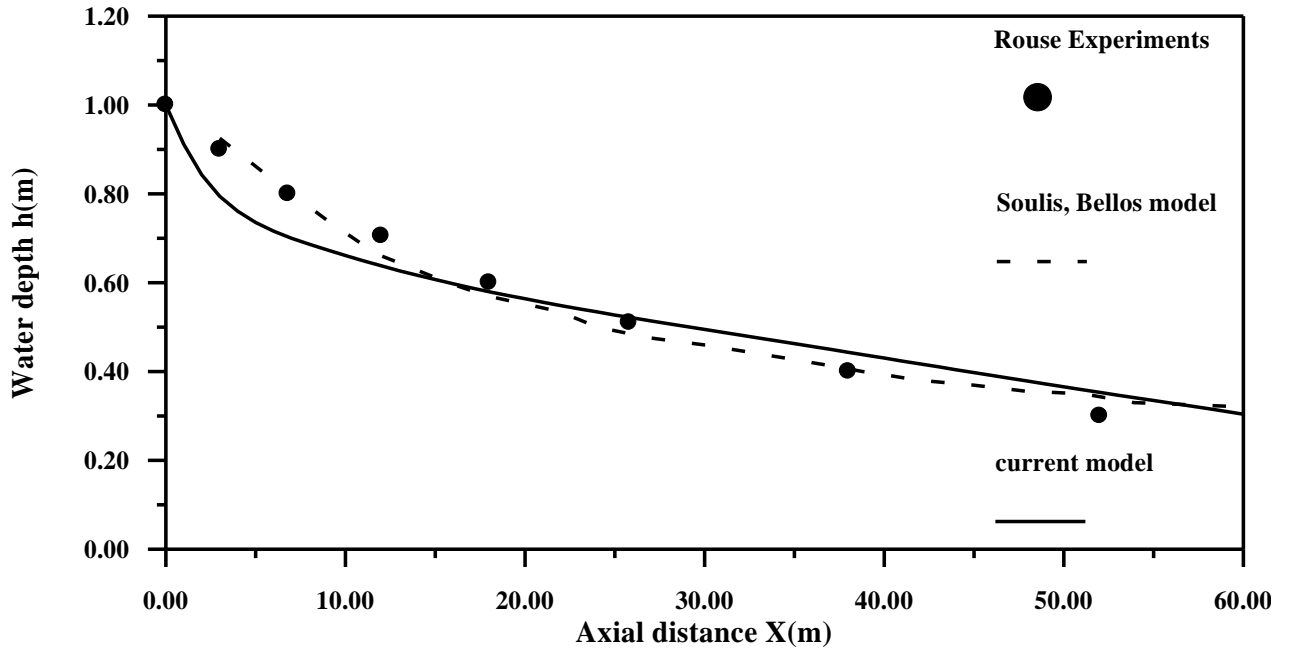


FIG. 12. WATER DEPTH COMPARISON BETWEEN CURRENT METHOD PREDICTIONS, MACCORMACK PREDICTIONS (SOULIS J. ET AL., 1989) AND MEASUREMENTS ALONG THE CURVED SIDE FOR THE ROUSE H. ET AL. (1951) CHANNEL AT  $Fr_1=4.0$

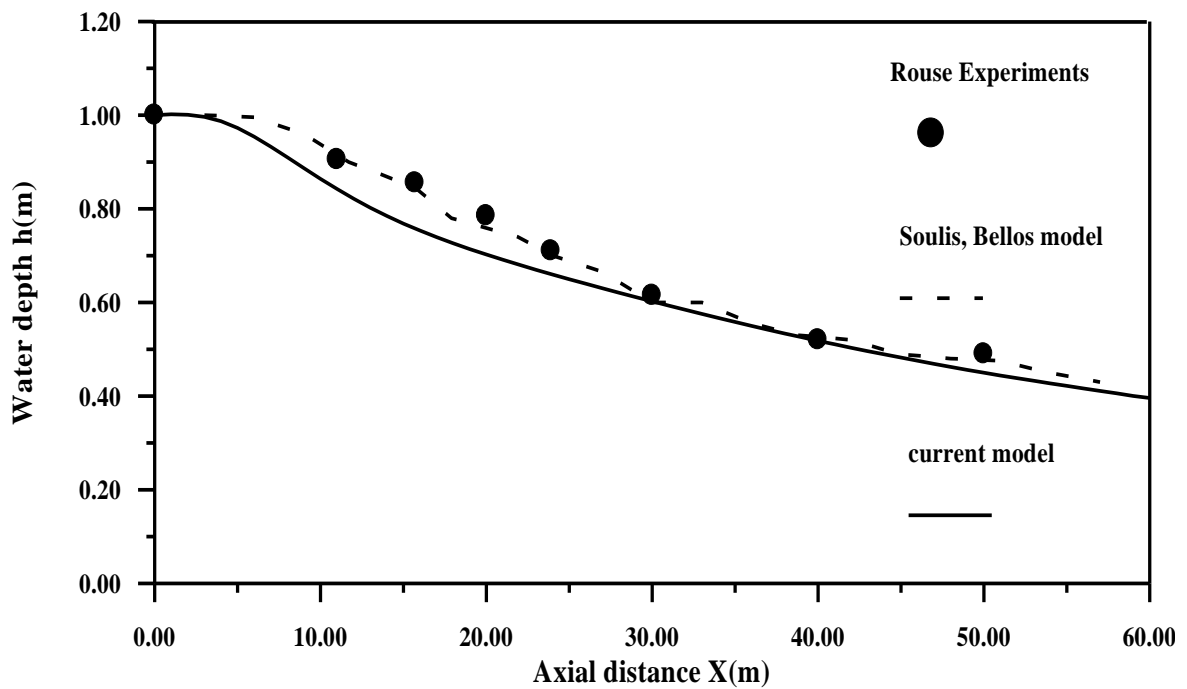
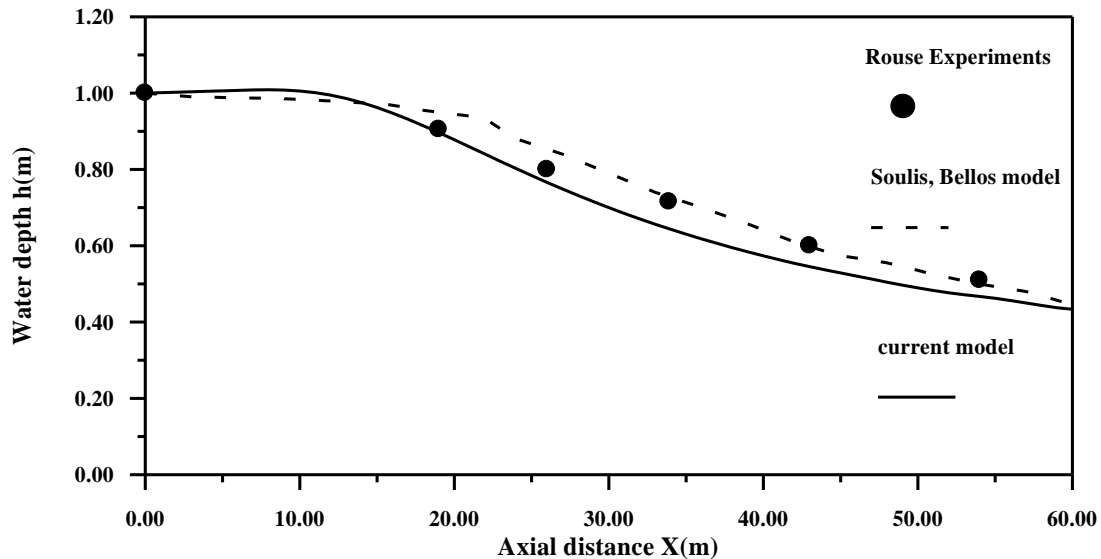


FIG. 13. WATER DEPTH COMPARISON BETWEEN CURRENT METHOD PREDICTIONS, MACCORMACK PREDICTIONS (SOULIS J. ET AL., 1989) AND MEASUREMENTS ALONG THE MID-STREAM LINE (LINE BETWEEN AXIS OF SYMMETRY AND CURVED SIDE) FOR THE ROUSE H. ET AL. (1951) CHANNEL AT  $Fr_1=4.0$



**FIG. 14. WATER DEPTH COMPARISON BETWEEN CURRENT METHOD PREDICTIONS, MACCORMACK PREDICTIONS (SOULIS J. ET AL., 1989) AND MEASUREMENTS ALONG THE FLUME AXIS OF SYMMETRY FOR THE ROUSE H. ET AL. (1951) CHANNEL AT  $Fr_1=4.0$**

## V. CONCLUSION

A depth-averaged, multi-grid, finite-volume, explicit, numerical scheme has been developed and subsequently applied to free-surface flow calculations. Main advantage of the proposed computational model is the ability to calculate subcritical and supercritical free-surface flow and to conform to physical boundaries of any open channel flow problem. The numerical approach is straight forward and the flow boundary conditions are easy enforced. The applied multi-grid acceleration technique gives very fast convergence. Application to a variety of open channel flow configurations is given to validate the method's potentialities. Applications regarding subcritical flow in a converging-diverging open channel and supercritical flow in a linearly expanding channel are reported. Comparisons with available measurements as well as with other numerical technique results show that the proposed method is a comparatively accurate and reliable technique. Very coarse grids give satisfactory comparison results. Free-surface flows simulation of practical interest in a straight forward way has been achieved. The method can be utilized for design computations.

## REFERENCES

- [1] Y. Chen, Z. Wang, Z. Liu and D. Zhu, (2012) "1D-2D Coupled Numerical Model for Shallow-Water Flows", Journal of Hydraulic Engineering", vol. 138, 2012, pp. 122-132.
- [2] E. Farsiroto, "Numerical and experimental study of scouring in alluvial channels", Ph.D. Thesis, 2000, Aristotle University of Thessaloniki, Civil Engineering Department, Thessaloniki, Greece.
- [3] K. Hoffmann and S. Chiang, "Computational Fluid dynamics for Engineers, 1993, Engineering Education System, Wichita, Kansas.
- [4] D. Hu, Y. Zhu, D. Zhong and H. Qin, "Two-Dimensional Finite-Volume Eulerian-Lagrangian Method on Unstructured Grid for Solving Advective Transport of Passive Scalars in Free-Surface Flows", Journal of Hydraulic Engineering, vol. 143, 2017, 04017051.
- [5] A. Kassem and M. Chaudhry, (1988) "Comparison of coupled and semi-coupled numerical models for alluvial channels", Journal of Hydraulic Engineering, ASCE, vol. 124, 1988, pp. 794-802.
- [6] H. Lien, T. Hsieh, J. Yang and K. Yeh, "Bend-Flow Simulation 2D Depth-Averaged Model", Journal of Hydraulic Engineering, vol. 125, 1999, pp. 1097-1108.
- [7] M. Liu, Y. Liu and W. Wei, "Numerical Simulation of 2D Flow in a Curved Channel", Advanced Materials Research, vol. 374-377, 2011, pp. 378-381.
- [8] T. Molls and M. Chaudhry, "Depth-averaged open channel flow model", Journal of Hydraulic Engineering, ASCE, vol. 121, 1995, pp. 453-465.
- [9] T. Molls, M. Chaudhry and K. Khan, "Numerical simulation of two-dimensional flow near a spur-dike", Advances in Water Resources, vol. 18, 1995, pp. 227-236.
- [10] T. Molls and G. Zhao, "Depth-Averaged Simulation of Supercritical Flow in Channel with Wavy Sidewall", Journal of Hydraulic Engineering, vol. 126, 2000, pp. 437-445.
- [11] A. Papanicolaou, M. Elhakeem and B. Wardman, (2011) "Calibration and Verification of a 2D Hydrodynamic Model for Simulating Flow around Emergent Bendway Weir Structures", Journal of Hydraulic Engineering, vol. 137, 2011, pp. 75-89.
- [12] H. Rouse, B. Bhoota and En-Yen Hsu, "Design of channel expansions", Transactions ASCE, vol. 116, 1951, pp. 347-363.

- 
- [13] J. Soulis and K. Bellos, "Steady, supercritical, open channel flow computations", Proc. 6th International Conference on Numerical Methods in Laminar and Turbulent Flow, Swansea, U. K., 1989.
- [14] J. Soulis J, "A Multi-grid method for open channel flow calculation", VIIIth International Conference on Computational Methods in Water Resources", Venice, Italy, 1990, pp. 221-230.
- [15] J. Soulis, E. Alexiou and E. Kounavas, "Measurements and computations of non- uniform flow", TechnikaChronika-A, vol. 11,1991, pp. 59-82.
- [16] J. Soulis, "A numerical method for subcritical and supercritical open channel flow", International Journal for Numerical Methods in Fluids, vol. 13, 1991, pp.437-464.
- [17] C. Yu and J. Duan, (2014) "Two-Dimensional Hydrodynamic Model for Surface-Flow Routing", Journal of Hydraulic Engineering, vol. 140, 2014, 04014045
- [18] H. Yu, G. Huang and C. Wu, "Efficient Finite-Volume Model for Shallow-Water Flows Using an Implicit Dual Time-Stepping Method", Journal of Hydraulic Engineering, vol. 141, 2015, 04015004
- [19] B. Yulistiyanto, Y. Zech and W. Graf, "Flow around a Cylinder: Shallow-Water Modeling with Diffusion-Dispersion" Journal of Hydraulic Engineering, vol. 124(4),1998, pp.419-429.

# New Formula for Lasik Surgery on Myopic & Hypermetropic Eyes

Prof.(Dr.) Bijay Kumar Parida (MBBS,LLB,MS,ICO,FRCSG)<sup>1</sup>, Ms.Anannya Anupurva<sup>2</sup>

<sup>1</sup>Associate Professor, Muthusamy Virtual University of Ophthalmology Post Graduation, Bhubaneswar, Odisha, India

<sup>2</sup>3<sup>rd</sup> year student, MVJ Medical College, Bangalore

**Abstract**— In this paper a new formula is derived for Lasik surgery on Myopic and Hypermetropic eyes. This article has given another formula to calculate the depth of cornea to be ablated, derived mathematically.

**Formula;**

depth of cornea of myopic eye to be ablated in micron =  $[r_1 \times D_1 \div D_2] - \sqrt{[r_2^2 - (d \div 2)^2]} \times 1000$

**Formula;**

depth of cornea in hypermetropic eye to be ablated on either sides in  $\mu = \frac{d}{2} - \sqrt{r_2^2 - [r_2 - [r_1 - \sqrt{r_1^2 - (\frac{d}{2})^2}]]^2} \times 1000$

**Keyword:** formula, LASIK, myopia, hypermetropia.

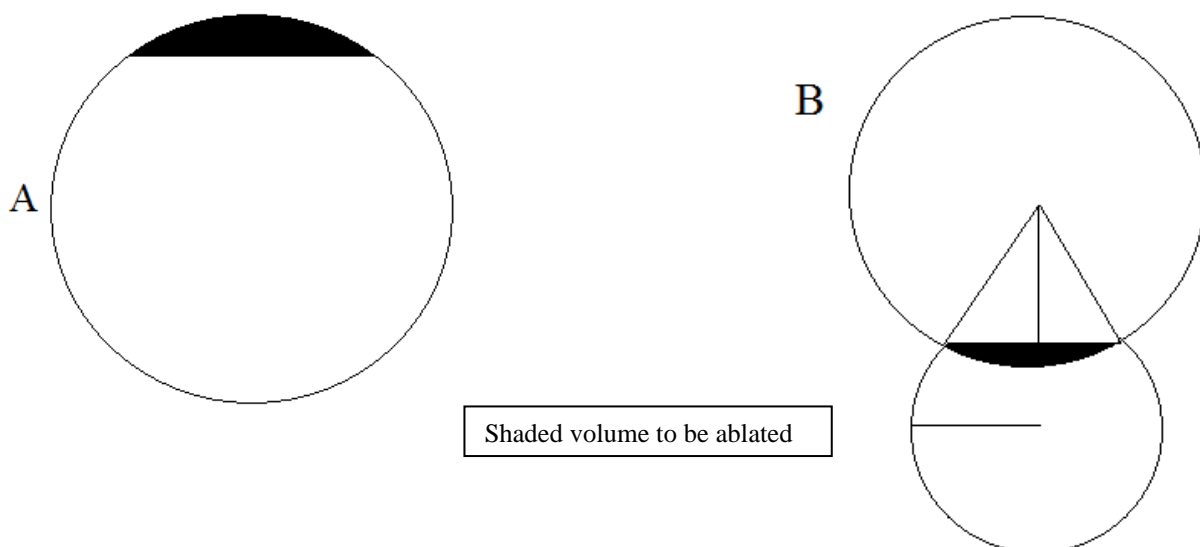
## I. INTRODUCTION

LASIK is acronym of laser assisted in situ keratomileusis. LASIK has become the standard approach for (corneal) refractive surgery by most ophthalmologists. Time has taught the refractive surgeon the omnious importance of doing a good surgical plan. Cornea is molded by laser. It's diameter of refractive surface either increased or decreased in order to increase or decrease the power of entire cornea. Charles Munnerlyn's <sup>[1] [2] [3]</sup> formula is used by lasik machine.

This article has given another formula to calculate the depth of cornea to be ablated, derived mathematically.

## II. OBSERVATION

Anterior surface of cornea



Anterior surface of cornea is responsible for refraction of ocular optical media, which is enormous, +49D<sup>[4]</sup> out of nearly total +60D of eye. LASIK has become the standard approach for corneal refractive surgery for most ophthalmologists. Its radius

of curvature is 7.45mm. So to reduce 4D of cornea, the power of anterior surface of cornea has to be 45D and radius has to be increased to  $(r_1 \times D_1) \div D_2$ .

$r_1$ =radius of curvature of anterior surface of cornea.

$r_2$ =radius of curvature planned,

$D_1$ =power of anterior surface of cornea.

$D_2$ = power of anterior surface of cornea planned.

$d$ =length of chord (diameter of cornea to be ablated)

$$r_2 = r_1 \times D_1 \div D_2$$

$$\text{chord} = \sqrt{r^2 - (d \div 2)^2}$$

#### Formula;

$$\text{depth of cornea of myopic eye to be ablated in micron} = [r_1 \times D_1 \div D_2] - [\sqrt{r_2^2 - (d \div 2)^2}] \times 1000$$

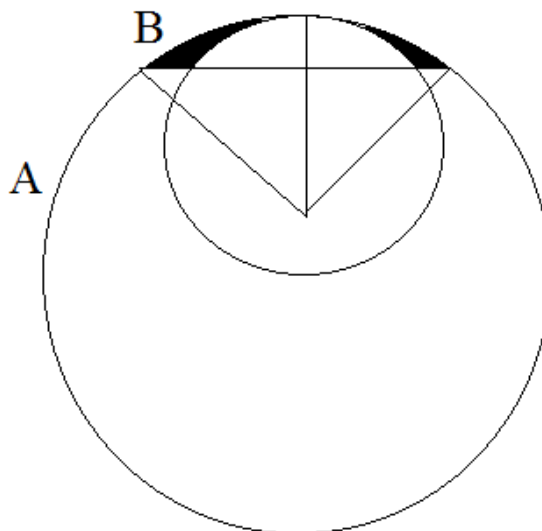
Example:  $r_1=7.45$  mm,  $r_2=91.2625$ ,  $d=4$ mm,  $D_1=+49$ D,  $D_2= - 4$ D

$$[7.45 \times 49 \div 4] - [\sqrt{91.2625^2 - 4/2^2}] \times 1000 = 91.2625 - 91.2406 = 0.0219 \times 1000 = \text{Depth in } \mu = 21.9$$

Munnerlyn's formula=depth to be ablated in micron= $(d^2 \times D) \div 3 = 21.33$

#### Formula for Lasik Surgery on Hypermetropic Eyes:

Radius of curvature of cornea is 7.45mm. This power has to be increased by 4D .The power of anterior surface of cornea is 49D [4]. The new power shall be 53D on anterior surface of cornea and radius has to be decreased to  $(r_1 \times D_1) \div D_2$ .



$r_1$ =radius of curvature of anterior surface of cornea .

$r_2$ =radius of curvature planned,

$D_1$ =power of anterior surface of cornea.

$D_2$  =new power of the anterior surface of cornea

Circle A is outer circle. circle B is inner circle. shaded part to be ablated.

1. Circle A is having radius  $r_1=7.45$ mm.

Diaptric power= $+49$ D.

So  $r_2=49 \times 7.45 \div 53=6.8877$ mm

2. Diameter (d1) or chord of 4mm from which ablation of stroma shall be done.
3.  $r_2=6.8877\text{mm}$
4. distance from chord to perimeter of circle= $r_1 - \sqrt{r_1^2 - (d_1 \div 2)^2}$  or  $7.45 - \sqrt{7.45^2 - 2^2} = 0.2735 \text{ mm}$
5. distance between chord and center of circle B=  $6.8877 - 0.2735 = 6.6142\text{mm}$
6.  $1/2$  of chord =  $\sqrt{6.8877^2 - 6.6142^2} = 1.9217 \text{ mm}$

Chord to be ablated on either sides as shaded area= $2 \cdot 1.9217 = 0.0783 \times 1000 = 78.3 \mu$

**FORMULA:** depth of cornea in hypermetropic eye to be ablated on either side in

$$\mu = \frac{d}{2} - \sqrt{r_2^2 - \left[ r_2 - \left[ r_1 - \sqrt{r_1^2 - \left( \frac{d}{2} \right)^2} \right] \right]^2} \times 1000$$

**Example**

$$4/2 - \sqrt{6.8877^2 - \left[ 6.8877 - \left[ 7.45 - \sqrt{7.45^2 - \frac{4^2}{2}} \right] \right]^2} \times 1000 = (2 - 1.9217) 1000 = 78.3 \mu$$

### III. DISCUSSION

Since 1949, Jose Barraquer Moner, described his Barraquer's thickness laws which states that whenever tissue is either added to the periphery of the cornea or removed from its central part, a corresponding flattening is obtained and vice versa, whenever tissue added to the center or removed from its periphery, a corresponding increase in curvature is obtained.<sup>[5][6]</sup>

Charles Mnerlyn in 1988 first published the article on formula for myopic eyes subjected to lasik surgery.<sup>[7][8]</sup>

Lasik surgery on hypermetropic eye is done by use of Gulani's triple lens. These are surgical acrylate polymer with marks of diameter 4.5mm, 4mm and 3.5 mm.<sup>[9]</sup>

The new formula written in this article exactly how much tissue in depth should be ablated on either sides of cornea with 120 micron flap.

If the chord is reduced to 3 mm, then 58.2  $\mu$  to be ablated. If flap size reduced to 100  $\mu$ , then the ablation is 40% of cornea at 540  $\mu$ . So 8D can be corrected which is safe and does not produce ectasia. The upper limit is 40%.

Formula is % of tissue to be ablated (PTA), flap thickness (FT), Ablation depth (AD), Central corneal thickness (CCT).

$$\text{PTA} = (\text{FT} + \text{AD}) / \text{CCT}.$$

For correction of 4D hyperopia, and diameter of cornea to be ablated is 4mm, 78.3 $\mu$  of cornea to be ablated per 1D correction  $78.3/4 = 19.6 \mu$  required.

If 3mm diameter of cornea is ablated, then  $78.3 \times 3 \div 4 = 58.8 \mu$  ablation can correct 4D. With thickness of flap 75 $\mu$  and thickness of cornea is 540  $\mu$  (40% of 540 = 216), only 216-75=141  $\mu$  can be ablated.  $(141 \div 58.8) \times 4 = 9.59 \text{ D}$  can be corrected and nearby cornea can be reshaped to 8.5D and 7.5 D till 5mm of diameter of cornea to avoid night glare.

Similarly, if myopic eye is corrected after raising a corneal flap of 75  $\mu$  and diameter of cornea ablated is 3mm, then 141 $\mu$  tissue can be ablated.  $(21.9 \times 3) \div 4 = 16.45 \mu$  ablation required to correct 4D. So  $(141 \div 16.45) \times 4 = 34.285 \text{ D}$  can be corrected. Night glare can be eliminated by tapering slowly the power by 1 D up to 6mm diameter of central cornea.

This is significant for correction of 6D in hypermetropia & 16D in myopia is targeted.

### IV. SUMMARY

**Formula;**

$$\text{depth of cornea of myopic eye to be ablated in micron} = [r_1 \times D_1 \div D_2] - [\sqrt{r_2^2 - (d \div 2)^2}] \times 1000$$



**Formula;**

$$\text{depth of cornea in hypermetropic eye to be ablated on either sides in } \mu = \frac{d}{2} - \sqrt{r_2^2 - \left[ r_2 - \left[ r_1 - \sqrt{r_1^2 - \left( \frac{d}{2} \right)^2} \right] \right]^2} \times 1000$$

**V. CONCLUSION**

New formulae for myopic and hypermetropic eyes for LASIK surgery are mathematically derived and shall definitely give better result if incorporated to lasik machine.

Correction of 1D myopia with 4mm diameter by ablating 5.475 $\mu$ .

Correction of hypermetropia with 4mm diameter by ablating 19.575  $\mu$  on one side.

Maximum possible correction of hypermetropia is 9.59D and of myopia is 34.285D with diameter of ablation at 3mm and flap thickness 75 $\mu$ .to avoid night glare the adjacent cornea must be gradually decreased in power of correction till diameter of 6mm of central cornea.

**REFERENCES**

- [1] Munnerlyn, CR, Koons, SJ, Marshall, J. "Photorefractive keratectomy: a technique for laser refractive surgery," J. Refract. Surg., 1988, 14, 46-52
- [2] Machat, JJ, "Fundamental Concepts and Principles of the Excimer Laser and LASIK" 1996, from The Art of LASIK, Second Ed., Machat, JJ, Slade, SG, Probst, LE eds, (Slack: Thorofare, NJ), Chapt 3, pg 33
- [3] Munnerlyn CR, Koons, SJ, Marshall, J. Photorefractive keratectomy: a technique for laser refractive surgery, J. Refract. Surg., 1988, 14, 46-52
- [4] Basic and clinical science course,section 3,clinical optics
- [5] Barraquer JJ. Queratoplastia Refractiva. Estudios e Informaciones. Oftalmologicas. 1949;2:10-30.
- [6] Barraquer JJ. Modification of refraction by means of intracorneal inclusions. Int Ophthalmol Clin. 1966;6(1):53-78.
- [7] Troutman RC,Swinger C;(1978),”REFRACTIVE KERATOPLASTY:Keratophakia and keratomileusis”Trans Am Ophthalmol Soc 76:329-39
- [8] Mc Donald MB,Kaufman HE,Franz TM,Shofner Salman B,Klyce SD(1989)”Excimer laser ablation-human eye”-Arch Ophthalmol.107(5):641-624 .
- [9] Waring Go 3<sup>rd</sup> .Development of a system for excimer laser corneal surgery.Trans Am Ophthalmol Soc 1989,87:854-983

# Reducing the Amount of Hard Drive Memory Used For Storing Elements of Abstract Data Types

Grigoriy Pronin<sup>1</sup>, Olga Popova<sup>2</sup>

Department of Information Systems and Programming, Kuban State Technological University, Russia

**Abstract**— This article proposes, presents and analyzes a new method of saving hard drive memory, used by Abstract Data Types. Abstract Data Types represents an important topic across a variety of application domains, but for several projects the method of memory allocation for the use of Abstract Data Types, presented in the built-in classes of the programming language C#, is not suitable by the reason of large possible memory loss. Method, reviewed in this article, can be implemented in other object-oriented programming languages. Sphere of application of represented method encompasses multiple types of Abstract Data Types, such as “list”, “stack”, “queue”, “deq” and several other. Implementation of reviewed solution requires usage of built-in class “array”. Realised classes become alternative patterns for built-in classes. The ways of usage of a new solutions is similar to the previous ones. Implementation of reviewed solution is done using Microsoft Visual Studio 2017. The results include theoretical conclusions drawn on the basis of practical research.

**Keywords**— Visual Studio 2017, Hard Drive Memory, Method, Abstract Data Type.

## I. INTRODUCTION

This article discusses the concept of abstract data types (ADT). Since the concept was formulated in 1974, abstract data types became an important part of the programming theory. Currently, the concept of ADT is one of the most popular methods of programming, along with the object-oriented programming.

### 1.1 Features of ADT

A distinctive feature of abstract data types is the fact that the functionality of the program component can be implemented in various ways. Different implementations of abstract data types are interchangeable.

"ADT is described by the mathematical theory of algebraic systems. Operations are implemented as functions of one or more parameters. A description of the operations, including a description of the argument types and return values, is called an algebraic system signature. Signatures represent a mathematical model of an abstract data type. This circumstance makes it possible to describe the functions of the program, specified by means of ADT, as algebraic systems" [1].

### 1.2 ADT in C#

"The C# programming language has many constructs that was borrowed from C++ and Java programming languages. However, it includes a number of new designs. Like the Java language, all instances of C# classes are dynamic objects and are hosted on a “heap”.

For all classes of predefined standard constructors, which provide the initial values of data. It is possible to add a number of new constructors that provide specific initialization of data elements, and any instance variable that is not initialized by an abstract constructor will receive a value from the standard constructor.

Destructors are also provided in C#, but they are rarely used because automatic garbage collection is used.

Structs or classes can be used to create ADTs in C#. The structures in C# differ significantly from their counterparts in C++. They can have constructors, properties, methods, data fields, and can implement interfaces but do not support inheritance.

A significant difference between structures and classes is that structures are value types and classes are reference types. Structures are placed on the stack, not on the heap. When used as parameters, structures are passed by value. All types-values in C#, including all primitive types, belong to structures. Instances of structures can be created by declaring them, like instances of other predefined value types, such as int or float. They can also be created using the new operator, which calls the constructor to initialize them." [2]

Structures are used to implement relatively small and simple types that will never be inherited. They are useful for creating objects that are placed on the stack (as opposed to the heap).

Three levels of access (public, private, and protected) in C# are specified by the same path as Java's.

### 1.3 Built-in ADT classes of C#

"Microsoft Visual Studio's C# has several built-in classes for realisation of different kinds of ADT. All the classes have the same structure, divided by the types of ADT. The difference of classes is in basic methods of their own, but the way of creation of a new variable for ADT's is the same: firstly, variable is created with only one element cell in it, but if program will identify this cell as filled cell, it will extend variable to the size that is equal to the previous one multiplied by 2" [3].

This method of variable creation has one big negative side: for example, if program uses a variable with 128 cells in it, built-in class of C# will extend this variable to the size of 256, because built-in class was created with a feature of saving extra cells for a new possible elements.

Creation extra cells is important, but even empty ones require memory to be stored, and in that case using built-in classes may lead to a loss of storage memory.

## II. METHOD

The next method have been implemented on C# programming language for class "stack" but the main idea of it can be used for any ADT on any programming language.

In this program, a class describing the stack was created manually. The beginning of the MyStack class shows that this class was implemented and developed on the basis of the built-in collection System.Array

```
class MyStack<T>
{
    T[] arr;
    public MyStack()
    {
        arr = new T[0];
    }
}
```

The Push method initially increases the stack size by 1, and then adds the specified element to the end of the array that the stack consists of:

```
public void Push(T item)
{
    Array.Resize(ref arr, arr.Length + 1);
    arr[arr.Length - 1] = item;
}
```

The Pop method is implemented by saving the last element of the stack and then reducing the stack size by 1:

```
public T Pop()
{
    T item = arr[arr.Length - 1];
    Array.Resize(ref arr, arr.Length - 1);
    return item;
}
```

The Makenull method is implemented through the built-in capability of the collection System.Array using a stack-size reduction loop until it is reduced to zero:

```
public void Makenull()
{
    for (int i = arr.Length; i > 0; i--)
    {
        Array.Resize(ref arr, arr.Length - 1);
    }
}
```

This solution of adding and deleting elements leads to using the exact needed size of ADT.

### III. RESULTS

The base class, showing a new method of creating Abstract Data Types, was implemented. The size of memory, used to store elements, was decreased. No compilation errors founded. All the tasks have been completed. The new method has shown the advantage in terms of hard drive memory saving.

#### 3.1 Program Code (C#)

```
using System;
using System.Collections.Generic;
using System.Linq;
using System.Text;
using System.Threading.Tasks;

namespace MyStack
{
class MyStack<T>
{
T[] arr;
public MyStack()
{
arr = new T[0];
}
public bool Empty
{
get
{
return arr.Length > 0;
}
}
public void Push(T item)
{
Array.Resize(ref arr, arr.Length + 1);
arr[arr.Length - 1] = item;
}
public T Pop()
{
T item = arr[arr.Length - 1];
Array.Resize(ref arr, arr.Length - 1);
return item;
}
public void MakeNull()
{
for (int i = arr.Length; i > 0; i--)
{
Array.Resize(ref arr, arr.Length - 1);
}
}
}
class Program
{
static void Main(string[] args)
```

```
{
MyStack<int> s1 = newMyStack<int>();
MyStack<int> s2 = newMyStack<int>();
for (int i = 0; i < 10; i++)
{
s1.Push(i);
Console.Write(i + " ");
}
Console.WriteLine();
for (int i = 10; i > 5; i--)
{
int a = s1.Pop();
s2.Push(a);
}
while (s1.Empty)
Console.Write(s1.Pop() + " ");
Console.WriteLine();
while (s2.Empty)
{
Console.Write(s2.Pop() + " ");
}
Console.WriteLine();
s2.Makenull();
Console.WriteLine();
while (s2.Empty)
{
Console.Write(s2.Pop() + " ");
}
Console.WriteLine();
for (int i = 0; i < 10; i++)
{
s2.Push(i);
Console.Write(i + " ");
}
Console.WriteLine();
}
}
```

#### IV. DISCUSSION

As a result, this method shown and proven itself as a good alternative to previous one. The size of memory, used to store elements, was decreased. As a negative side has been founded a small increase of RAM usage, but using multithreaded core can solve this problem. That way, previewed method is recommended for use on big projects with many elements in it, while Microsoft Visual Studio's solution is recommended for use on small number of elements. In that case, both methods proven their usability, but both of them also have negative sides.

#### V. CONCLUSION

As a result, this method shown and proven itself as a good alternative to previous one. The size of memory, used to store elements, was decreased. Accumulated experience confirmed the extensibility solution of the Abstract Data Types and encouraged further exploration within other application domains, such as saving information and tables file creation. The article have revealed a proprietary mechanism that was closely related with the Abstract Data Types approach for specifics of object-oriented type of programming. Therefore, the article considered the implementation of the new way of saving memory

in the context of crating files using Abstract Data Types, especially for Microsoft Visual Studio soft.

#### **ACKNOWLEDGEMENTS**

I have been fortunate to work with Olga Popova, talented lecturer that inspired and influenced this research. Studies of this bright person let me knowledge about Abstract Data Types, terms of its usage and its structure. Lections and practical studies under her guidance and supervision had shown me the best way of using my own knowledge and abilities of searching for and discovering new aspects of programming. I am very thankful that I had luck to be her student.

#### **REFERENCES**

- [1] Rod Stevens, (2016). Algorithms-theory and practical application (Linked list. Stacks and queues.). Moscow.: E publishing house, 544 p.
- [2] Pavlovskaya T. A., (2009). C#. Programming in a high-level language. St. Petersburg: Peter, 432 p
- [3] Microsoft MSDN open resource

# New Formula to Calculate the Size of the Corneal Flap for Autologous Ipsilateral Rotational Keratoplasty

Prof.(Dr.) Bijay Kumar Parida (MBBS,LLB,MS,ICO,FRCSG)<sup>1</sup>, Ms.Anannya Anupurva<sup>2</sup>

<sup>1</sup>Associate Professor, Muthusamy Virtual University of Ophthalmology Post Graduation, Bhubaneswar, Odisha, India

<sup>2</sup>3<sup>rd</sup> year student, MVJ Medical College, Bangalore

**Abstract**— A new formula for autologous ipsilateral rotational keratoplasty has been designed and verified by surgical procedure on 19 eyes. The formula is found to be successful in all cases. The diameter (D) of the cornea to be rotated is equal to the length of scar from one side of pupillary margin in semidark room, nearest to the scar to the farthest end of the scar (L) nearest to center of pupil, added to the pupillary diameter (Pd) in semidarkness. The direction of rotation of scar is just opposite of radius under consideration and off center by 0.5mm (trephine is put on 0.5mm outside the pupillary margin).

$$D=L+Pd$$

Minimum clear cornea required for rotational flap is 4 mm on one side of the pupil. In eyes with eccentric corneal opacities partially involving the pupillary area, using a rotational corneal autograft, can revitalise vision. This procedure does not warrant immunological rejection associated with allografts.

**Keywords**— rotational autograft, cornea, formula.

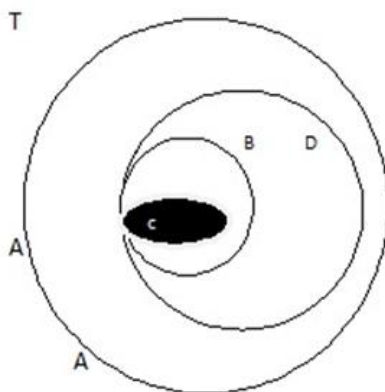
## I. INTRODUCTION

Many erudite authors have prescribed formulae for this purpose. But two of them shall be discussed in the chapter for discussion, as it is commonly used. Formula have been described that help assess the suitability of the procedure and choose the size of the trephine to be used. The use of digital photographs and imaging software to assess the suitability of the procedure has also been described by other learned authors<sup>[1,2,3]</sup>. This is a procedure that works best in eyes that have a central corneal opacity and clear peripheral cornea. An eccentric trephination is performed that allows the removal of disk of cornea containing the central opacity.

Various methods have been described for these calculation<sup>[4,5]</sup>.

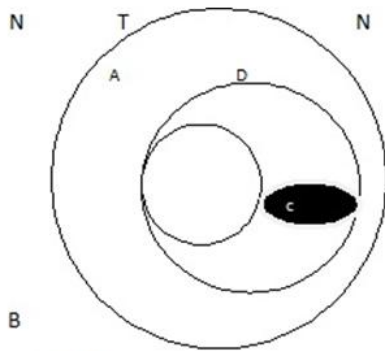
## II. MATERIAL & METHOD

19 cases were operated having corneal scar involving either entire pupil or a part of the pupil. The scars were of variable thickness, either involving entire thickness of the cornea or partial thickness of cornea. The age of the patients ranged from 10 years to 44 years. The formula mentioned above was followed to use size of the trephine.



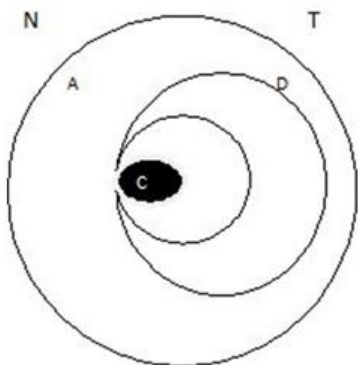
- A . Cornea of size = 12mm in diameter.
- B. Pupil size of diameter =4mm
- C. Scar involving 3mm of temporal side of pupil
- D. Planned rotation of flap=3mm+4mm=7mm in diameter.
- T. Temporal side
- N. Nasal side

**FIGURE 1A: LEGENDS (MONO IMAGES)**



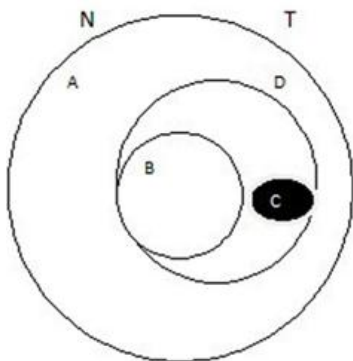
**After rotation of corneal flap**

- A . Cornea of size = 12mm in diameter.
- B. Pupil size of diameter = 4mm
- C. Scar is out of pupil and driven to temporal side
- D. Planned rotation of flap=3mm+4mm=7mm in diameter.
- T. Temporal side
- N. Nasal side



- A . Cornea of size = 12mm in diameter.
- B. Pupil size of diameter =4mm
- C. Scar involving 2mm of temporal side of pupil
- D. Planned rotation of flap=2mm+4mm=6mm.

**FIGURE 2A**



**After rotation of corneal flap**

- A . Cornea of size = 12mm in diameter.
- B. Pupil size of diameter =4mm
- C. Scar is out of pupil and driven to temporal side
- D. Planned rotation of flap=2mm+4mm=6mm.

**FIGURE 2B**

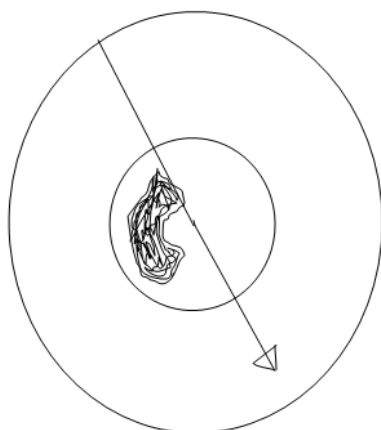


**FIGURE 3A: ROTATION OF FLAP**  
 SHADED AREA IS THE SCAR BEFORE ROTATION

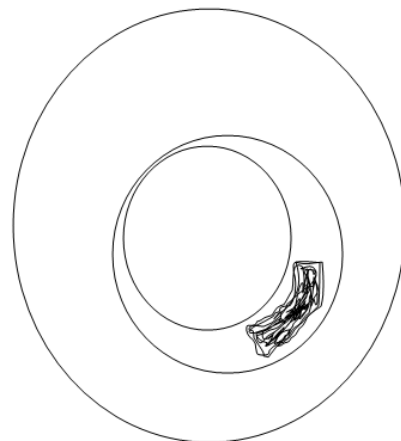


**FIGURE 3B: AFTER ROTATION, POSITION OF SCAR**



Suturing was done first by smooth apposition of epithelium at 4 points. Then the needle grazes over either descemet's membrane or stroma depending on thickness of cornea to continue smooth apposition of epithelium.

Follow ups after 1 month and 6 months were done to evaluate visual acuity and endothelial count by specular microscope at graft junction and other parts of rotated cornea were done. In average postoperative visual acuity was 6/12 and endothelial count was satisfactory. Night glare was absent in all cases.

It was concluded that this formula to select the size trephine was satisfactory.

### III. DISCUSSION

Formula proposed by Dr Jonas is  $\frac{3}{4}$  diameter of the cornea- $\frac{1}{2}$  e(preoperative distance between the corneal center and nearest edge of the opacity to the center)<sup>[1]</sup>.

Example- figure 1 if cornea diameter is 12 mm, then  $\frac{3}{4} \times 12 = 9$ mm.

Scar size 3mm (2 mm on nasal side and 1 mm on temporal side of center of pupil).

Then  $\frac{1}{2}$  of 1mm=1/2mm

$9 - \frac{1}{2} = 8.5$ mm

\*Applying proposed formula designed by Dr Bijay, 3mm+4mm=7mm flap of cornea needs to be rotated starting from nasal side of the cornea. Thus it is found that flap size is 1.5 mm less than the flap size required by the formula designed by Dr Jonas. Larger flap leads to closeness to limbus. This may initiate rejection of cornea and invasion of blood vessels into cornea. "A rotational autograft can be an effective alternative to standard penetrating keratoplasty for some patients with corneal scars. We establish a mathematical model for most clinical instances of a rotational autograft, in which an 8-mm graft with a decentration of 0.5 mm best satisfies the goals of surgery. Studies assure that the endothelial loss due to such procedure is less in comparison to homologous penetrating keratoplasty<sup>[6]</sup>.

It means that 8mm of diameter of graft is used in all cases.

\*By formula of Dr. Bijay, only 7mm of diameter of cornea is rotated.

Autokeratoplasty using the contra lateral eye has been used relatively infrequently because the set of circumstances that indicate this procedure are rare (i.e, the patient must have a nonfunctioning control at real eye with a clear cornea)<sup>[7-10]</sup>.

Several authors have suggested the use of different geometric shapes for the ipsilateral autokeratoplasty, such as a triangle<sup>[11-13]</sup>, a rectangle<sup>[14]</sup> or a figure eight<sup>[11-13]</sup>; how-ever, none have replaced the standard circular graft with an eccentric center<sup>[17-21]</sup>. In this form of penetrating keratoplasty, the area of clear cornea is placed in the geometric center of the cornea and the opacity is rotated toward the limbus. The objective is to achieve the largest possible optically clear zone.

### IV. CONCLUSION

The new formula for autologous ipsilateral rotational keratoplasty is shown below

$$D=L+Pd$$

Which is very simple and verified by surgical procedure on 19 eyes.

It is expected to give successful result with suturing at differential thickness of cornea as thickness of new alignment is not equal.

### REFERENCES

- [1] Bourne WM, Brubaker RF. A method for ipsilateral rotational autokeratoplasty. *Ophthalmology*. 1978;85:1312-1316
- [2] Karpouzas I, Pouliquen YJ-M. Computerized method for rotational autokeratoplasty. *Cornea*. 1991;10:369-371.
- [3] Jonas JB, Panda-Jonas S. Calculation of size and location of autologous ipsilateral rotating keratoplasty. *Graefes Arch Clin Exp Ophthalmol*. 1994;232:538-544
- [4] Bourne WM, Brubaker RF. A method of ipsilateral rotational autokeratoplasty. *Ophthalmology*. 1978;85:1312-1316
- [5] McDonnell pj, Falcon MG. Rotational autokeratoplasty. *Eye*. 1989;3:576-580
- [6] Optimal Size and Location for Corneal Rotational Autografts A Simplified Mathematical Model Natalie A. Afshari, et al. *Arch Ophthalmol*, / VOL 124, MAR 2006.p410-413

- [7] Gundersen T, Calnan AF. Corneal autografts, ipsilateral and contralateral. *Arch Ophthalmol*. 1965;73:164-168.
- [8] Stocker FW. Rotating autokeratoplasty. *SouthMedJ*. 1969;62:1183-1184.
- [9] Boruchoff SA, Dohlman CH. Corneal autografts. *Am J Ophthalmol*. 1967;63:1677-1681.
- [10] Groden LR, Arentsen JJ. Ipsilateral rotating autokeratoplasty. *Ann Ophthalmol* 1982;15:899-901.
- [11] Forster A. A review of keratoplastic surgery and Some experiments in keratoplasty. *Am J Ophthalmol*. 1923;6:366-375.
- [12] McDonnell PJ, Falcon MG. Rotational autokeratoplasty. *Eye*. 1989;3:576-580.
- [13] Mortada A. Rectangular autogenous penetrating keratoplasty. *Am J Ophthalmol* 1965;59:795-799.
- [14] Wilson RS. "Figure 8" ipsilateral autokeratoplasty. *Arch Ophthalmol*. 1976;94:121-122.
- [15] Vasco-Posada J. Ipsilateral autokeratoplasty. *Am J Ophthalmol*. 1967;64:717-721.
- [16] Sah WJ, Myoung YW, Hahn TW, Kim JH. Rotational autokeratoplasty in advanced lipid keratopathy. *Ophthalmic Surg Lasers*. 1997;28: 1020-1024. *Exp Ophthalmol*. 1994;232:538-544.
- [17] Gillette TE, Nebres DW. Computer modeling of rotational autokeratoplasty. In: Cavanagh HD, ed. *The Cornea: Transactions of the World Congress on the Cornea* New York, NY: Raven Press; 1988:237-240.
- [18] Menezo JL, Taboada JF, Cisneros AL, Ferrer E. Rotational autograft, reconstruction of the anterior segment, and intraocular lens implantation. *J Cataract Refract Surg*. 1986;12:146-149.
- [19] Verma N, Melengas S, Garap JA. Ipsilateral rotational autokeratoplasty for the management of corneal opacities. *AustNZJ Ophthalmol*. 1999;27:21-25.
- [20] Miller D, Wolf E. A model for comparing the optical properties of different-sized corneal grafts. *Am J Ophthalmol*. 1969;67:724-728.
- [21] Gradle HS. The present status of keratoplasty. *Am J Ophthalmol*. 1921;4:895-899

# Value-at-Risk of JCP Stock and Analysis of Calendar Effects

Xinyan Zhang<sup>1</sup>, Rong Zhang<sup>2</sup>

<sup>1</sup>Department of Statistics and Mathematics, Inner Mongolia University of Finance and Economics, Hohhot, Inner Mongolia, 010070, P. R. China

<sup>2</sup>Department of Mathematics and Statistics, University of Massachusetts, Amherst MA 01003, USA

**Abstract**— This paper presents the value-at-risk (VaR) analysis of J.C. Penney Company Inc. (JCP) stock daily negative log returns between 1993 and 2018. The statistical properties of JCP are thoroughly examined and a series of diagnostic tests are conducted to check the conditions of the time series data over the two decades. The GARCH and EGARCH models with normal distribution and Student's *t*-distribution are used to estimate the volatility and VaR of the stock. By analyzing VaR, we show that there is currently a high risk of investing in JCP stock. In addition, this paper examines the calendar effects and seasonality of JCP stock through the fundamental properties of the data as well as the VaR. We compare the performance of the stock in four quarters which further confirms our result that JCP stock is at immense risk at this point in time. These results are valuable for anyone interested in evaluating and forecasting JCP stock. The methodology we use is applicable to any other stock that meets our test conditions and is more accurate and realistic in predicting volatility and VaR than the commonly used standard normal distribution based VaR model.

**Keywords**— JCP Stock, Value-at-Risk, GARCH Model, EGARCH Model, Calendar Effect.

## I. INTRODUCTION

Over the past two decades, the proliferation of the Internet has contributed to the development of e-commerce and has affected the market share of traditional retailers. Purchasing goods online as a convenient alternative to in-store shopping largely saves people's time and is increasingly popular among customers. J.C. Penney Company Inc. is a US department store chain that operates more than 1000 stores across the United States. It was founded by James Cash Penney and William Henry McManus [1] in 1902. Most J.C. Penney stores are located in shopping centers, and their business mainly includes sales of clothing, cosmetics, household items, jewelry and cookware. As J.C. Penney is one of the largest apparel and home retailers in the United States, investors are deeply concerned about the performance of J.C. Penney Company Inc. stock (NYSE: JCP). In this paper, we will investigate the risk of buying JCP stock as well as the calendar effects of the JCP stock returns. We want to provide investors with useful investment advice.

In 2017, Caroline, Emma, Madelon, Mikkel and Marc from Columbia Business School conducted a research project on J.C. Penney named "*Competing for Survival: A Turnaround of Department Store J.C. Penney*" [2]. They analyzed the company's performance from an operational perspective and provided a variety of strategies to help the company better organized. So far, we have found a lack of statistical analysis of J.C. Penney's paper. In this paper, we conducted a complete time series analysis of the JCP stock returns. We focus on the statistical characteristics of JCP stock and draw conclusions only from the statistics.

Risk management is a key process for making investment decisions. In order to control risk in an investment, we need to first determine the amount of risk involved in the investment, and then decide to either accept or alleviate the risk. Standard deviation, beta, value at risk (VaR) and expected shortfall are common measures to quantify the risk. In this paper, we use VaR as the primary tool for measuring the risk of buying stocks. Value-at-risk is a statistical indicator of the riskiness of financial entities or portfolios. It is defined as the maximum dollar amount that is expected to be lost at a predetermined confidence level for a given time frame. The stock market crash in 1987 triggered the innovation of VaR. It was developed as a systematic approach to separating extreme events from daily price changes. In 1994, it was extended by J.P. Morgan who launched the Risk Metrics and published the methodology [3]. Nowadays, VaR has become one of the most commonly used measures of market risk in the financial industry.

In order to calculate the VaR of the stock, we need to accurately predict the price of the stock. The main characteristic of a stock is its return. We model the negative log return series to derive estimates of volatility and VaR. It is well known that financial markets are highly volatile and the periods of high volatility tend to persist for some time before the market returns to a more stable environment (Tsay,2005)[4]. The autoregressive method helps to build a more accurate and reliable volatility model. The Autoregressive Conditional Heteroskedasticity (ARCH) model was originally introduced by Engle

(1982)[5]. ARCH model and its extensions such as GARCH (Bollerslov, 1986)[6] and EGARCH (Nelson, 1991) [7] are among the most popular models for forecasting market returns and volatility. See for example Vesna Bucevska (2013)[8], Zhen Yao Wong et al. (2016)[9], Julija Cerović Smolović et al. (2017)[10] and Mahsa Gorji, Rasoul Sajjad (2017) [11], who derived VaR estimation from GARCH - type models.

In terms of the organization of the paper, we analyze the basic statistical properties of the time series of negative log returns for JCP in Section 2, and test for the normality and autocorrelations of the series. In Section 3, we fit the data with GARCH and EGARCH models and estimate the VaR of the data. In Section 4, we group the data by quarter and perform time series analysis within the group, and then we analyze the results for each group to find calendar effects

## II. DATA DESCRIPTION AND STATISTICAL TEST RESULTS

### 2.1 Data Description

In this paper, we examine the daily JCP stock price time series for a 25-year period. There were 6431 data points from January 29, 1993 to August 10, 2018. All data comes from Yahoo Finance. Let  $P_t$  denote the daily adjusted closing price of a stock, where  $t$  is an integer representing the day. We use the negative log return  $L_t$  to characterize the stock price time series.  $L_t$  is defined as:

$$L_t = -100 \cdot \log \frac{P_t}{P_{t-1}} = 100(\log P_{t-1} - \log P_t) \quad (1)$$

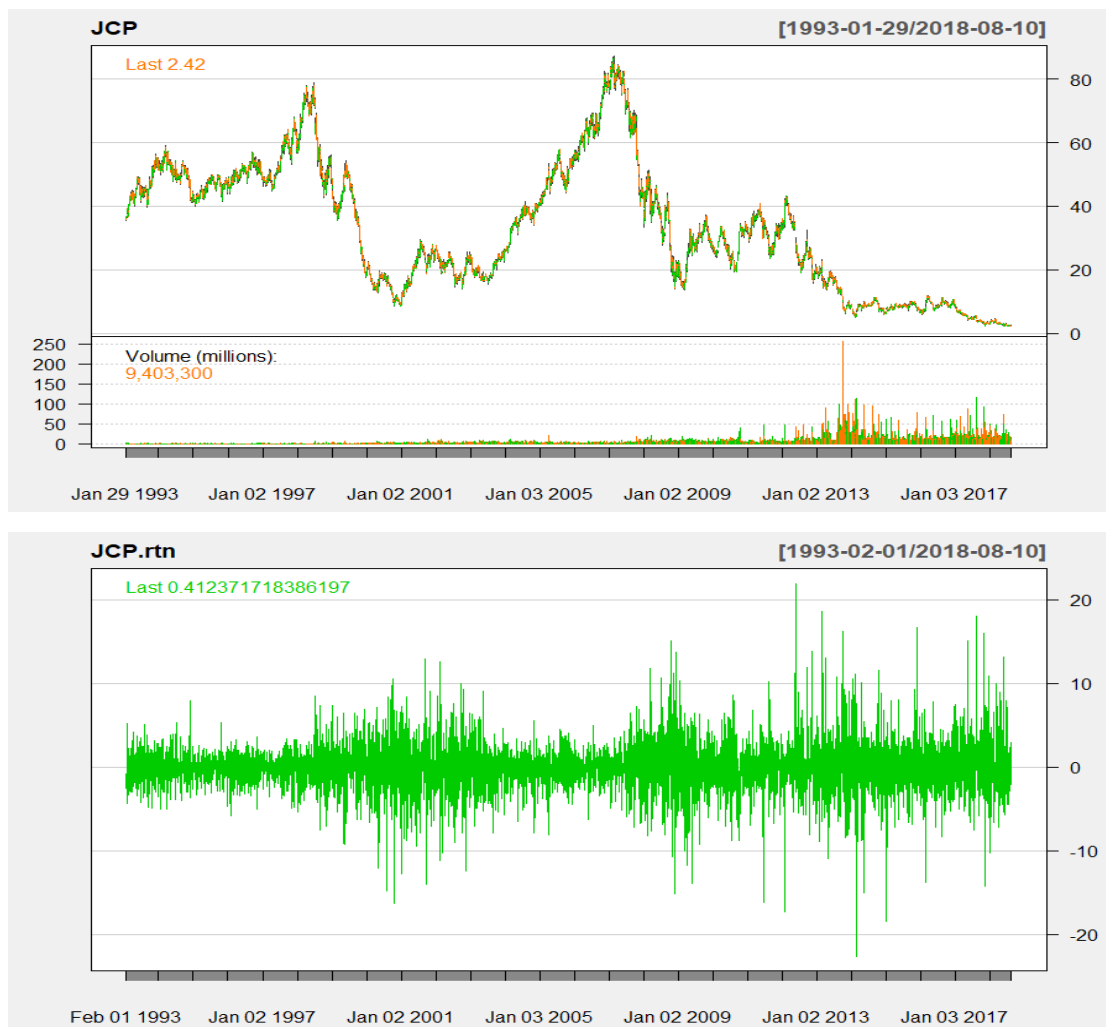
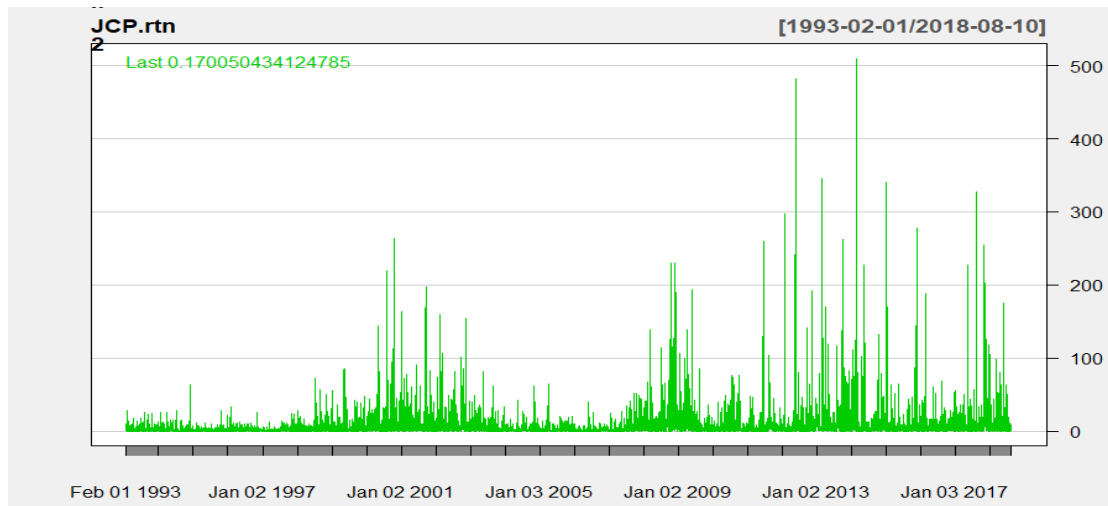


FIGURE 1: The upper panel is adjusted closing price for JCP; the lower panel is daily negative log returns



**FIGURE 2: The daily squared log returns for JCP**

The lower panel in Fig. 1 shows the time series plot of daily negative log returns for JCP stock. We can see from the graph that roughly from 2013 to 2018, there are more peaks in the upper half of the panel. Since we model relative loss instead of relative return, more positive peaks indicate more positive relative loss of the stock. Fig. 2 shows the time series plot of daily squared log returns of JCP stock. It can be seen that since 2011, the stock has become more volatile than before, and the stock volume shown in Fig. 1 has become higher after 2011. There are a lot of documented evidence of high stock trading volume closely related to the volatility of returns; see for example Barron, Ori E., David G. Harris, and Mary Stanford (2005[12]), K. Ravichandran, Sanjoy Bose (2012 [13]), Andrey Kudryavtsev (2017[14]).

From the price chart in Fig. 1, JCP stock reached its highest price in 2007 and then fell sharply in the following year. From 2012 to 2018, the stock price has a clear downward trend, but the trading volume tends to be higher and there are more peaks during this period. This may indicate potential activities such as stock news, analyst downgrades and insider trading.

**TABLE 1  
SUMMARY STATISTICS OF THE DAILY NEGATIVE LOG RETURNS FROM FEB. 1, 1993 TO AUG. 10, 2018**

	Mean	Range	Std dev	Skewness	Kurtosis	Nobs
JCP	0.032	(-22.582,21.962)	2.814	0.031	5.561	6430

Table 1 summarizes the fundamental properties of daily negative log return series of JCP stock. It gives us a better view of the performance of JCP stock. It shows a positive average daily negative log return of 0.032, which indicates a positive relative loss on average.

**TABLE 2  
SUMMARY STATISTICS OF THE DAILY NEGATIVE LOG RETURNS GROUPED BY YEAR**

Time	Mean	Range	Std dev	Skewness	Kurtosis	Nobs
1993.1.29-1998.8.10	-0.051	(-5.791,8.487)	1.588	0.006	1.606	1396
1998.8.11-2008.8.10	0.008	(-16.217,12.981)	2.707	-0.344	3.064	2514
2008.8.11-2018.8.10	0.105	(-22.582,21.962)	3.391	0.179	4.766	2518

Table 2 shows the summary statistics of the daily negative log returns for JCP stock that are grouped into three time periods. From August 11, 2008 to August 10, 2018, the average daily negative log return is 0.105 which is the highest among the three periods. It is apparent that the average daily negative log return increases at a high rate over time. In addition, in the most recent decade, the range of the daily negative log returns is the largest, from -22.582 to 21.962, with a standard deviation of 3.391, which indicates high volatility of the stock.

**2.2 Test for normality**

To test for the normality of the data, we use the Q-Q (quantile-quantile) plot to see if the empirical distribution of the daily negative log returns is consistent with the normal distribution.

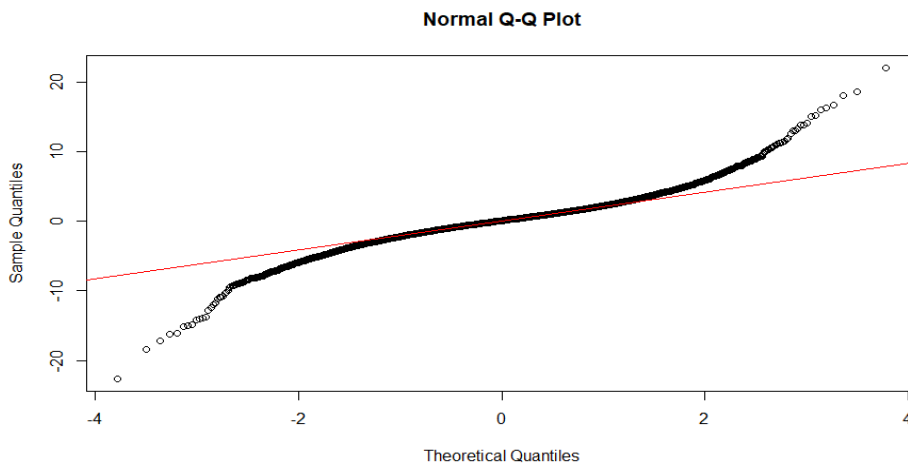


**FIGURE 3: Q-Q plot of the daily negative log returns for JCP against normal distribution**

Fig. 3 is a Q-Q plot of the empirical distribution of the daily negative log returns (y-axis) against normal distribution (x-axis). It can be observed from the plot that the empirical distribution of the daily negative log returns displays heavier tails than the normal distribution. Therefore, normal distribution is not an ideal fit for the negative log returns.

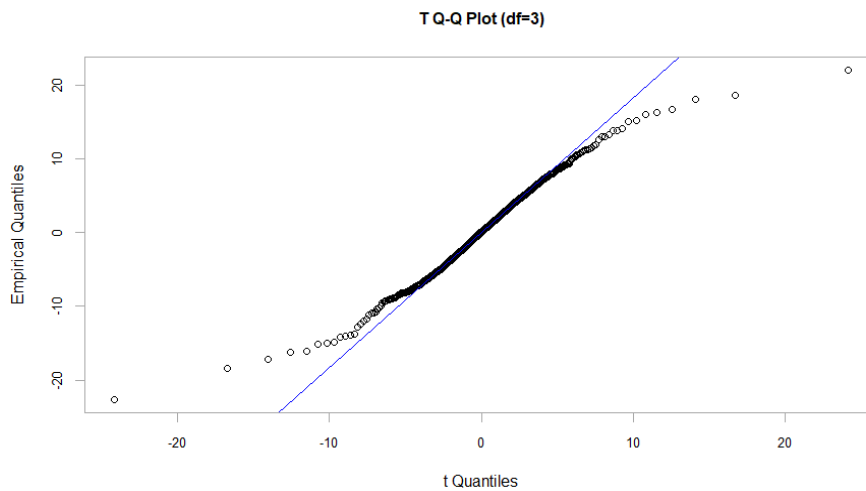


**FIGURE 4: Q-Q plot of the daily negative log returns for JCP against Student’s t-distribution**

We also test the empirical distribution of the daily negative log returns against the Student’s t-distribution using Q-Q plot. From Fig. 4, we can see that with degrees of freedom of 3, the empirical distribution of the daily negative log returns has lighter tails than the Student’s t-distribution. It is apparent that the Student’s t-distribution is a much better fit for the negative log returns.

To confirm our results, we perform Shapiro-Wilk normality test (1965) [15] to check for the normality of daily negative log returns for JCP. The results are shown below.

**TABLE 3  
SHAPIRO-WILK NORMALITY TEST OF DAILY NEGATIVE LOG RETURNS FOR JCP**

Statistic	p-value	Test Result
W = 0.95186	<2.2e-16	The series does not come from normal distribution

From Table 3, we can see that the p-value from this test is extremely small. For a significance level of 0.05, we reject the null hypothesis that the data comes from a normal distribution. This is consistent with our result from the Q-Q plot.

**2.3 Test for autocorrelations**

The autocorrelation coefficient (ACF) and the partial autocorrelation coefficient (PACF) are very important for us to check the specifications of the model used in analyzing the data. With the presence of autocorrelations, we can use autoregressive-moving-average (ARMA) models to fit the data. The ACF and PACF graphs for JCP negative log returns and squared log returns are shown in Fig. 5. From the graphs, we can see that the daily negative log return series exhibits weak autocorrelations, whereas the squared log return series have indication of strong autocorrelations.

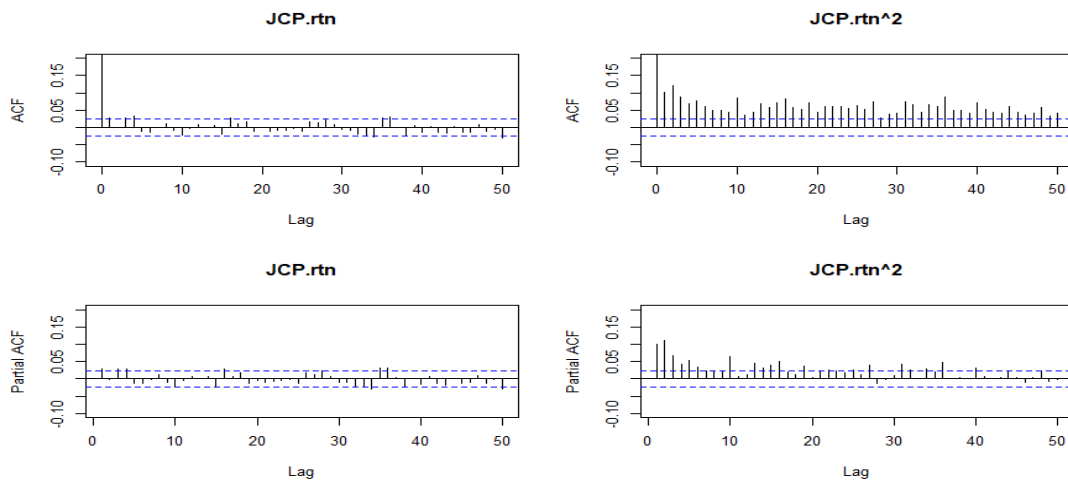


**FIGURE 5: Sample ACF and PACF for JCP daily negative log returns and squared log returns**

In order to confirm the results, we use the Ljung-Box test devised by Ljung and Box (1978) [16] to test the autocorrelations of the negative log return series and the squared log return series. The Ljung-Box test statistic is usually represented by  $Q(m)$ , where  $m$  is the number of lags tested. If the test statistic  $Q(m)$  is greater than  $\chi^2_\alpha$  or the p-value from the test is smaller than the significance level of  $\alpha$ , we reject the null hypothesis that the data are independently distributed and conclude that the data exhibits autocorrelations.

The Ljung-Box test results are displayed in Table 4. The p-values are small for daily negative log returns and extremely close to zero for daily squared log returns at lags of 5, 10 and 15. At significance level of 0.05, we reject the null hypothesis and conclude that there are strong autocorrelations within our data.

**TABLE 4  
LJUNG-BOX TEST FOR JCP DAILY NEGATIVE LOG RETURNS AND SQUARED LOG RETURNS**

m	Daily Negative Log Returns		Daily Squared Log Returns	
	$\chi^2$ -squared	p-value	$\chi^2$ -squared	p-value
5	17.287	0.003986	279.51	<2.2e-16
10	23.141	0.01024	395.42	<2.2e-16
15	26.14	0.03658	501.98	<2.2e-16

From the above statistical tests, we can see that the negative log return series  $\{L_t\}$  has non-normality and relatively strong autocorrelations. For time series with these properties, a powerful test - the ARCH test was introduced by Engle (1982) to evaluate the significance of ARCH effects of the data, see [4]. Here we perform the ARCH test in Table 5. We can see that the p-values for daily negative log return series are very small at lags of 5, 10 and 15. Therefore, we reject the null hypothesis at significance level of 0.05 and conclude that there are significant ARCH effects in our data.

**TABLE 5**  
**ARCH TEST FOR JCP DAILY NEGATIVE LOG RETURNS AND SQUARED NEGATIVE LOG RETURNS**

m	Daily Negative Log Returns		Daily Squared Log Returns	
	$\chi$ -squared	p-value	$\chi$ -squared	p-value
5	41.76	<2.2e-16	0.8852	0.4899
10	25.23	<2.2e-16	0.5928	0.8212
15	18.95	<2.2e-16	0.4136	0.9761

### III. VALUE AT RISK WITH GARCH AND EGARCH MODEL

#### 3.1 Methodology

ARCH model was proposed by Engle (1982) [4] to deal with the model's time-varying volatility and heteroskedasticity of the errors. It was extended by Bollerslev (1986)[6] to the generalized autoregressive conditional heteroskedasticity (GARCH) model. The GARCH model is used to approximate conditional variance using a linear function of the past squared residuals. The model still has some shortcomings because it ignores the leverage effect of return volatility. To reflect the asymmetry of returns, we applied the EGARCH model proposed by Nelson (1991) [7], in which the volatility can react asymmetrically to positive and negative returns.

Let  $\{L_t\}$  be the daily negative log returns of JCP stock as defined in Section 1 and  $\{F_t\}$  be the past information about the return series up to time t. Since there is volatility and leptokurtosis in the data, we assume that the conditional mean of  $\{L_t\}$  follows an autoregressive average model AR (1) and the conditional variance of  $\{L_t\}$  follows an univariate GARCH model or EGARCH model. We represent  $\{L_t\}$  as follow:

$$\begin{cases} L_t = \mu_t + \sigma_t \varepsilon_t \\ \mu_t = \phi_0 + \phi_1 L_{t-1} \end{cases} \quad (2)$$

the innovation  $\{\varepsilon_t\}$  are white noise process with zero mean and unit variance, and we assume  $\sigma_t^2$  follows a GARCH-type model. In this paper, we assume  $\{\varepsilon_t\}$  to follow normal and Student's t-distribution respectively. The conditional mean  $\mu_t$  is defined as:  $\mu_t = E(L_t | F_{t-1})$ , and the conditional variance  $\sigma_t$  is defined as:  $\sigma_t^2 = Var(L_t | F_t)$ .

The GARCH (p, q) model is given by:

$$\sigma_t^2 = \alpha_0 + \sum_{j=1}^p \alpha_j \eta_{t-j}^2 + \sum_{i=1}^q \beta_i \sigma_{t-i}^2, \text{ for } p, q > 0 \quad (3)$$

where  $\eta_t = \sigma_t \varepsilon_t$ , p is the order of GARCH and q is the order of ARCH process,  $\alpha_j$  and  $\beta_i$  are parameters and we expect their sum to be less than 1.

We use GARCH (1, 1) model and EGARCH (1, 1) model to fit the data. Petra Posedel (2005) [18], Richard A. Ashley and Douglas M. Patterson (2010)[19], Joel koima, Peter N Mwita, and Dankit K Nassiuma (2015) [20] have shown that the basic GARCH(1, 1) model is sufficiently suitable for most financial time series. From equation (3), we can easily get the equation for the GARCH (1, 1) model:

$$\sigma_t^2 = \alpha_0 + \eta_{t-1}^2 + \beta_1 \sigma_{t-1}^2 \quad (4)$$

The EGARCH (p, q) model is given by the following formula:



$$\log \sigma_t^2 = \alpha_0 + \sum_{j=1}^p [\alpha_j \eta_{t-j} + \gamma_j (|\eta_j| - E|\eta_{t-j}|)] + \sum_{i=1}^q \beta_i \log \sigma_{t-i}^2, \text{ for } p, q > 0 \quad (5)$$

From equation (5), we derive the EGARCH (1, 1) model:

$$\log \sigma_t^2 = \alpha_0 + \eta_{t-1} + \gamma_1 (|\eta_{t-1}| - E|\eta_{t-1}|) + \beta_1 \log \sigma_{t-1}^2 \quad (6)$$

The results of fitting data using GARCH and EGARCH models are illustrated in Table 6. The log likelihood  $\log(L)$  shows that the serial correlations in the conditional means and variances are sufficiently explained by the specified GARCH and EGARCH models. The positive coefficient  $\gamma_1$  in the EGARCH model implies the presence of a leverage effect.

**TABLE 6**  
**ESTIMATION RESULTS IN GARCH AND E GARCH MODELS FOR JCP**

GARCH type	GARCH Model		EGARCH Model	
	Normal	Student's t	Normal	Student's t
$\phi_0$	-0.041362	0.004727	-0.000560	0.021645
$\phi_1$	0.012557	0.002382	0.007003	-0.001397
$\alpha_0$	0.010825	0.018960	0.009296	0.008382
$\alpha_1$	0.023102	0.031519	0.046362	0.039226
$\beta_1$	0.975893	0.966760	0.996278	0.995399
$\gamma_1$			0.048972	0.065170
$\log(L)$	-15080.79	-14763.57	-14995.24	-14719.55

### 3.2 Estimation of VaR

After fitting the data with GARCH and EGARCH models, we are able to predict the volatility of the daily negative log returns for JCP. We then proceed to estimate the value at risk (VaR) of the stock. As introduced in Section 1, VaR is a popular method of measuring risk of an investment, because it is easy to interpret and clearly a relevant concept in assessing the risk. It represents the maximum dollar amount that is expected to be lost at a predetermined confidence level for a specific period of time. In this study, we calculate the VaR by the quantile method. Let  $\{L_t\}$  be the daily negative log returns of JCP stock and  $\alpha$  be the confidence level.  $VaR_\alpha$  is the  $\alpha$ -th quantile of the distribution of the negative log returns  $\{L_t\}$ , and is defined by:

$$P(L_t > VaR_\alpha(L_t)) \leq 1 - \alpha \quad (7)$$

**TABLE 7**  
**FORECAST VALUE AT RISK IN GARCH AND E GARCH MODELS ON AUG. 13TH, 2018 FOR JCP AND SPY**

	GARCH type	GARCH Model		EGARCH Model	
		Normal	Student's t	Normal	Student's t
JCP	$VaR_{0.95}$	4.924947	4.355218	5.1341	4.523923
	$VaR_{0.99}$	6.980224	7.256845	7.26029	7.440851
	$VaR_{0.999}$	9.283975	12.66881	9.643528	12.71962
SPY	$VaR_{0.95}$	0.8465751	0.7579894	0.9715966	0.8895356
	$VaR_{0.99}$	1.237037	1.303512	1.399687	1.472815
	$VaR_{0.999}$	1.674705	2.253133	1.879532	2.443175

From the skewed property of the negative log return data, the Student's t-distribution should fit better for the distribution of white noise  $\{\varepsilon_t\}$ . To make comparisons, we use both normal and Student's t-distributions to test the VaR. Table 7 demonstrates the results for one-day-ahead VaR (on August 13, 2018) for JCP at quantiles 0.95, 0.99 and 0.999 respectively. To make comparisons, we also calculate one-day-ahead VaR (on August 13, 2018) for SPDR S&P 500 trust (SPY) [21] stock of which the results are shown in the same table. SPY is an exchange-traded fund (ETF) used to track the S&P 500 stock market index. It is the largest ETF in the world and represents all major sectors of the US market. From Table 7, it is clear that JCP has much higher VaR than SPY for the three quantiles.

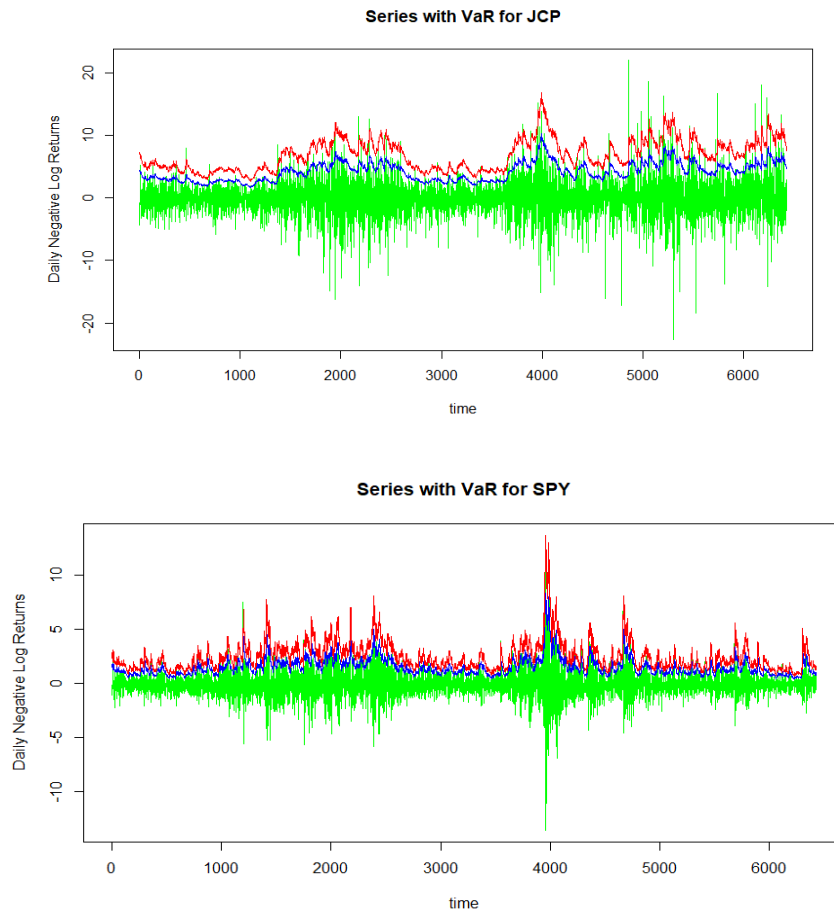


**FIGURE 6: One-day-ahead VaR forecast of JCP and SPY based on the EGARCH model with Student's t-distribution at quantile 95% in blue and 99% in red**

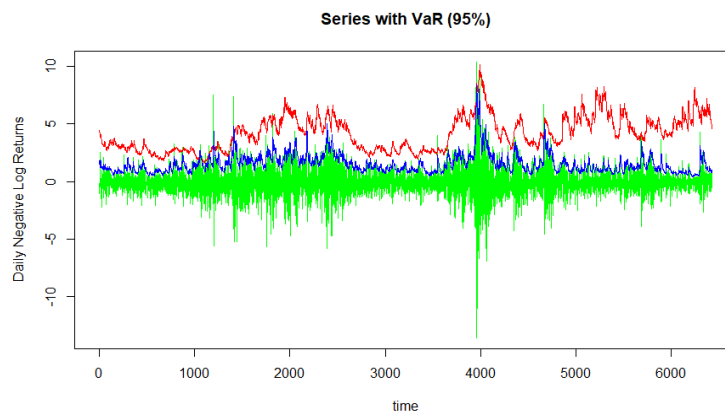


**FIGURE 7: One-day-ahead VaR forecast based on the EGARCH model with Student's t-distribution at quantile 95%, with JCP in red and SPY in blue**

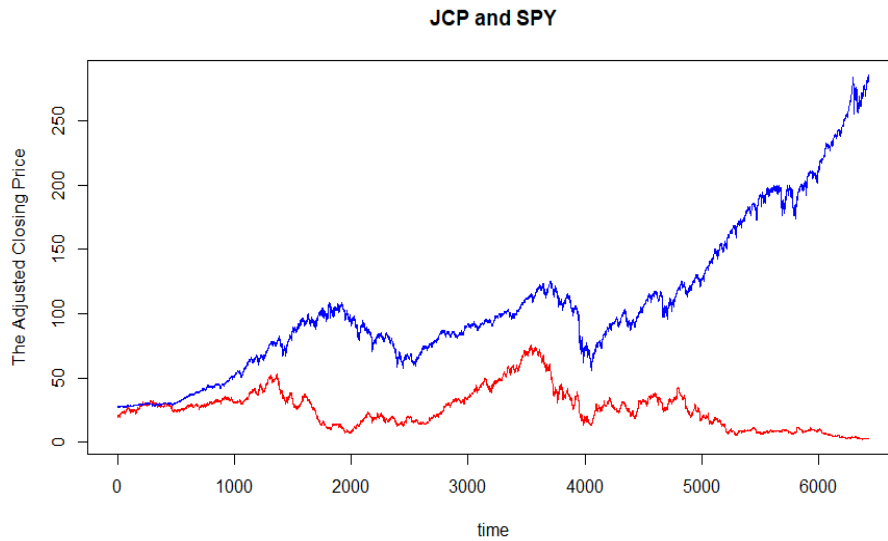


**FIGURE 8: Adjusted Closing Price for JCP in red and SPY in blue**

From Fig. 7, it is clear that on most of the days, JCP has much larger VaR than SPY. In addition, the VaR of JCP stock becomes higher and deviates further from the VaR of SPY in recent years. Fig. 8 shows a comparison graph of the adjusted closing price for JCP stock and SPY stock. As the price of SPY increased since 2010, the price of JCP displayed a decreasing trend. Combining the analysis of the VaR and the price plot of JCP, we find that JCP stock is highly risky for investment.

**IV. CALENDAR EFFECT**

A calendar effect [22] is an economic effect that seems to be associated with the calendar. If the returns of a stock vary from season to season, it is said to have seasonal tendencies and calendar effect. In order to investigate any calendar effect of JCP stock, we divide our data into four groups on a quarterly basis. Each quarter contains three months, the first quarter includes January to March expressed as Q1, the second quarter includes April to June expressed as Q2, and so on.

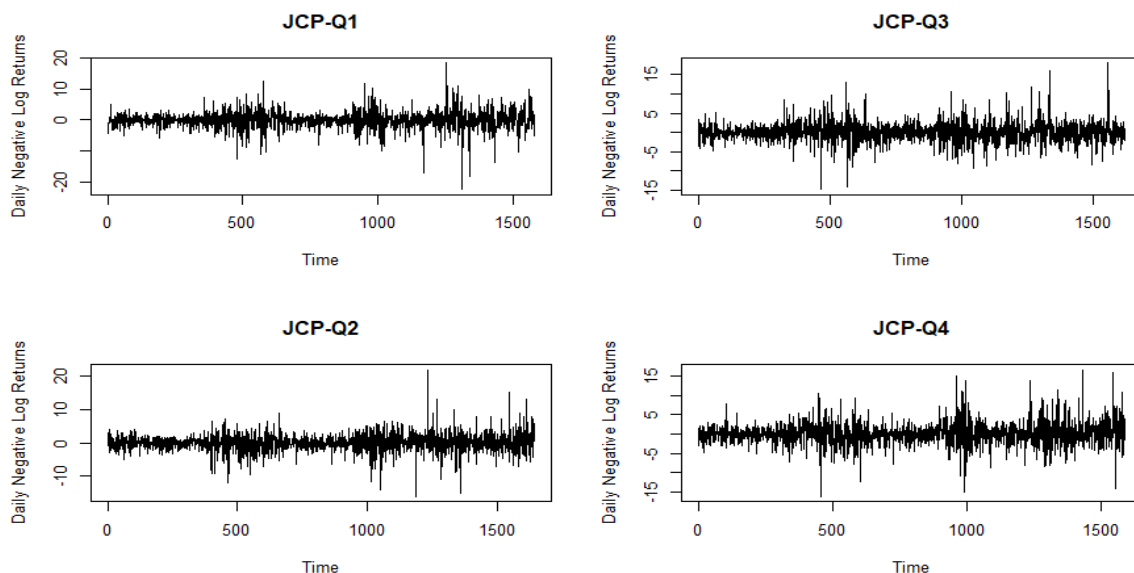


**FIGURE 9: The adjusted closing price for four quarters of JCP**

Fig.9 shows the time series plots of the daily negative log returns for the four quarters. From the graphs, we can see that the negative log returns of the fourth quarter Q4 are the most volatile among the four quarters. Furthermore, there are many large positive peaks in Q4, especially from time of 1200 and more, which indicates that in recent years, JCP stock experienced a lot of losses in Q4.

**TABLE 9**  
**SUMMARY STATISTICS OF THE DAILY NEGATIVE LOG RETURNS FOR JCP BY QUARTER**

	Mean	Range	Std dev	Skewness	Kurtosis	Observation
Q1	-0.068	(-22.582,18.592)	2.884	-0.440	6.851	1579
Q2	-0.008	(-16.101,21.962)	2.689	0.040	6.524	1643
Q3	0.124	(-14.813,18.105)	2.663	0.342	4.904	1618
Q4	0.080	(-16.217,16.674)	3.011	0.218	3.888	1590

Table 9 shows the summary statistics of the daily negative log returns for the four quarters. From the table, we can see that in the third and fourth quarter Q3 and Q4, JCP stock has positive average daily negative log return with that in Q3 to be the largest. It indicates that JCP stock generally experiences loss in Q3 and Q4. Although the average daily negative log return in the first and second quarter Q1 and Q2 is negative, the magnitude is relatively small.

After checking the normality and autocorrelations of the data for the four quarters, we fit the data of each quarter with GARCH and EGARCH models based on normal distribution and Student's t-distribution respectively. Then we calculate one-day-ahead VaR at quantile 95% and 99% respectively of the stock negative log returns for each quarter. The results are shown in Table 10.

**TABLE 10**  
**VALUE AT RISK OF FOUR QUARTERS IN GARCH AND EGARCH MODELS FOR ONE-DAY-AHEAD PERIOD**

	GARCH type	GARCH Model		EGARCH Model	
	Distribution	Normal	Student's t	Normal	Student's t
Q1	$VaR_{0.95}$	5.5055	5.1341	6.0122	5.6980
	$VaR_{0.99}$	7.8419	8.8800	8.5437	9.6957
Q2	$VaR_{0.95}$	6.3523	5.9994	7.2951	6.4139
	$VaR_{0.99}$	9.0205	10.126	10.3406	10.7452
Q3	$VaR_{0.95}$	3.6436	3.2475	3.6474	3.3087
	$VaR_{0.99}$	5.1297	5.5203	5.1112	5.5915
Q4	$VaR_{0.95}$	6.9963	6.6221	6.8536	6.5923
	$VaR_{0.99}$	9.8818	10.9387	9.6649	10.7553

From Table 10, the third quarter Q3 has the smallest VaR for both 95% and 99% quantiles, while the fourth quarter Q4 exhibits the largest VaR for both quantiles with Student's t assumption. The VaR for the first and second quarter Q1 and Q2 is large as well, despite the negative average daily negative log return in Q1 and Q2 shown in Table 9. Therefore, none of the four quarters performs well, because none of them exhibits both positive average log return and stability. Furthermore, it is an interesting phenomenon that JCP has positive average relative loss and high risk in Q4, because Q4 is usually the best season for traditional retailers to make money. It implies that JCP is not competitive with traditional retailers, which supports our previous analysis that JCP has a high investment risk.

## V. CONCLUSION

In this paper, we analyze the fundamental statistics and the VaR of the daily negative log returns of JCP stock. We use GARCH and EGARCH models to fit the data with normal distribution and Student's t-distribution assumptions of white noise respectively. Based on the models, we estimate VaR of the stock at quantiles 95%, 99% and 99.9% to measure the riskiness of the stock. Comparing the VaR of JCP and SPY, we find that the VaR of JCP stock is much higher than SPY, and the price of JCP is significantly lower than SPY, especially in the past ten years. The summary statistics also indicates that

the daily negative log returns of JCP averaged over ten-year period increased over time and reached the highest during the past ten years. These results help us conclude that the risk of investing in JCP stock is very high.

By analyzing the calendar effect of JCP, we find that although the returns in the four quarters are different, the performance of the stock is not good for either of the four quarters. It is surprising that Q4 has positive average daily negative log return and the highest one-day-ahead VaR among the four quarters. In general, for traditional retailers, the fourth quarter should be the most profitable, because Thanksgiving and Christmas are at the end of the year, and all goods have great discounts during the festivals. The fourth quarter is usually the quarter that Americans spend the most. However, even in the fourth quarter, J.C. Penney cannot make a profit either. It even suffered losses during Q4 and had the highest VaR in a year. It reinforces our previous conclusion that JCP is at immense risk for investment.

### ACKNOWLEDGEMENTS

The first author is supported by the National Nature Science Foundation of China, No. 11561050, the Natural Science Foundation of Inner Mongolia, No. 2016BS0103, the Science and Technology Plan Projects of Inner Mongolia, No. NJZY16143, and the National statistical science research project, No. 2015LY27.

### REFERENCES

- [1] (2018) <https://www.britannica.com/biography/J-C-Penney> [Online]
- [2] Columbia Business School Turnaround Management Final Project. 2017.  
<https://turnaround.org/sites/default/files/7.%20Paper%20-%20JCPenney.pdf> [Online]
- [3] (2018) [https://en.wikipedia.org/wiki/Value\\_at\\_risk](https://en.wikipedia.org/wiki/Value_at_risk). [Online]
- [4] Ruey S. Tsay. Analysis of Financial Time Series, Second Edition. Wiley, 2005.
- [5] Robert F. Engle, "Autoregressive Conditional Heteroscedasticity with Estimates of the Variance of United Kingdom Inflation," *Econometrica*, Vol. 50(4), pp. 987-1007, Jul. 1982.
- [6] Tim BOLLERSLEV, "GENERALIZED AUTOREGRESSIVE CONDITIONAL HETEROSKEDASTICITY," *Journal of Econometrics*, Vol. 31, pp. 307-327, 1986.
- [7] Daniel B Nelson, "Conditional Heteroskedasticity in Asset Returns: A New Approach," *Econometrica*, vol. 59(2), pp. 347-370, 1991.
- [8] Vesna Bucevska, "An Empirical Evaluation of GARCH Models in Value-at-Risk Estimation: Evidence from the Macedonian Stock Exchange," *Business Systems Research*, Vol. 4(1), pp. 49-64, March 2013.
- [9] Zhen Yao Wong, Wen Cheong Chin, Siow Hooi Tan, "Daily value-at-risk modeling and forecast evaluation: The realized volatility approach," *The Journal of Finance and Data Science*, Vol. 2, pp. 171-187, 2016.
- [10] Julija Cerović Smolović, Milena Lipovina-Božović, Saša Vujošević, "GARCH models in value at risk estimation: empirical evidence from the Montenegrin stock exchange. *Economic Research-Ekonomska Istraživanja*," Vol. 30(1), pp. 477-498, 2017.
- [11] Mahsa Gorji, Rasoul Sajjad, "Improving Value-at-Risk Estimation from the Normal EGARCH Model," *Vizja Press & IT*, Vol. 11(1), pp. 91-106, 2017.
- [12] Barron, Ori E., David G. Harris, and Mary Stanford, "Evidence That Investors Trade on Private Event-Period Information around Earnings Announcements," *The Accounting Review*, Vol. 80, pp. 403-421, Apr. 2005.
- [13] K. Ravichandran, Sanjoy Bose, "Relationship Between Stock Return and Trading Volume," *Research Journal of Business Management*, Vol. 6(1), pp. 30-39, 2012.
- [14] Andrey Kudryavtsev, "The Effect of Stock Return Sequences on Trading Volumes," *International Journal of Financial Studies*, Vol. 5(4): 1-15, 2017.
- [15] Samuel S. Shapiro, Martin B. Wilk, "An Analysis of Variance Test for Normality (Complete Samples)," *Biometrika*, Vol. 52(3/4), pp. 591-611, Dec. 1965.
- [16] Greta M. Ljung, Geoege E. P. Box, "On a measure of lack of fit in time series models," *Biometrika*, Vol. 65(1), pp. 297-303, Aug. 1978.
- [17] Bollerslev, Tim, Hylleberg, Svend, "A NOTE ON THE RELATION BETWEEN CONSUMER'S EXPENDITURE AND INCOME IN THE UNITED KINGDOM," *Oxford Bulletin of Economics and Statistics*, Vol. 47(3), 1985, pp. 153-170.
- [18] Petra Posedel, "Properties and Estimation of GARCH(1,1) Model," *Metodološki zvezki*, Vol. 2(2), 2005, pp. 243-257.
- [19] Richard A. Ashley, Douglas M. Patterson, "A TEST OF THE GARCH(1, 1) SPECIFICATION FOR DAILY STOCK RETURNS," *Macroeconomic Dynamics*, Vol. 14(1), pp. 137-144, 2010.
- [20] Joel koima, Peter N Mwita, Dankit K Nassiuma, "VOLATILITY ESTIMATION OF STOCK PRICES USING GARCH METHOD," *Kabarak Journal of Research & Innovation (KJRI)*, Vol. 3(1), pp. 48-53, 2015.
- [21] <https://us.spdrs.com/en/etf/spdr-sp-500-etf-SPY> [Online]
- [22] [https://en.wikipedia.org/wiki/Calendar\\_effect](https://en.wikipedia.org/wiki/Calendar_effect) [Online]

# Biological Removal of Nitrogen and Phosphorus using Activated Sludge Treatment in Meat Processing Wastewaters

Anisa Myrtaj (Rexhepi)<sup>1</sup>, Acad. Assoc. Ilirjan Malollari<sup>2</sup>

<sup>1</sup>Department of Chemistry, Faculty of Technical Sciences, "Ismael Qemali" University, Vlora, ALBANIA

<sup>2</sup>Department of Industrial Chemistry, Faculty of Natural Sciences, Tirana University, Tirana, ALBANIA

**Abstract**—The main purpose of this study was to identify the best treatment techniques for wastewater discharged from meat processing. The organic matters in the meat industry wastewater are considerable and complex. To identify the organic component of wastewater we use the parameters to classify it. The most common parameters are the oxygen demand values. We have evaluated the two most common oxygen demand methods, the biochemical oxygen demand and the chemical oxygen demand. In this investigation thorough pretreatment studies were done using the activated sludge treatment.

*This treatment was performed at optimal pH using different dosages of activated sludge.*

*Minimization of wastewaters discharges consist on keeping under continuous control: the quality of wastewaters; their treatment and disposal in an environmentally manner, optimization of processes, maintenance and respective design.*

**Keywords**—Wastewater, activated aludge, treatment, COD, BOD<sub>5</sub>.

## I. INTRODUCTION

The processing of meat and meat by-products requires large quantities of potable water, and nearly all of this is discharged as high strength organic, nutrient (nitrogen and phosphorus), fat and microbial contaminated effluent. Many of the processing plants are rural based and therefore require on-site treatment with discharge limits that are becoming tighter as community expectations increase for better treated wastewater discharges, especially into surface water.

The meat industry has to deal with a number of environmental challenges. This includes responsible wastewater treatment and disposal to prevent land and waterpollution. A well designed and managed wastewater treatment system is essential to achieve regulatory requirements and help protect and maintain a sustainable environment.

By focusing on reducing water usage, optimize wastewater treatment and improved waste management, both disposal and treatment costs can be reduced.

Biological wastewater treatment is often associated with secondary wastewater treatment and intends to treat the dissolved and colloidal organics after primary treatment. The goal of all biological wastewater treatment systems is to coagulate and remove or reduce the nonsettling organic solids and the dissolved organic load from the effluents by using microbial communities to degrade the organic load. Biological wastewater treatment is generally a major part of secondary treatment design of wastewater and characterized by reduction of the oxygen demand of an influent wastewater to a given level of purification. The microorganisms responsible for reducing the organic matters and consequently the oxygen demand of incoming wastewater can be classified in aerobic and anaerobic.

Aerobic biological treatment dominates secondary wastewater treatment and is performed in the presence of oxygen by aerobic microorganisms. From a nutritional point of view, the majority of microorganisms in biological wastewater treatment systems use the organic matters in the wastewater as the energy source for growth and maintenance of microorganisms.

Anaerobic processes are also used in the secondary biological treatment of wastewater. Anaerobic processes, in addition to sludge digestion, are employed to treat high-strength wastewater, such as food-processing wastewater streams.

## II. WASTEWATER CONSTITUENT

In the wastewater stream has inevitably some blood, fat, manure, meat and detergents. These wastes contribute to the key constituents, which are described below:

- Organics: comprising BOD, COD, TSS, oil and grease - are generally biodegradable. If the wastewater is not managed well its degradation by bacteria can cause odours.

- Nitrogen (in organic, ammonia and oxidised forms) and Phosphorous (typically in the form of organic P or phosphate) are essential nutrients for living organisms. Abattoir effluent contains high levels of both. The degree of treatment required depends on the final disposal route. River disposal requires almost complete removal of both.
- pH is typically neutral and temperatures can vary from cool to hot. High temperatures (greater than 38°C) can enable fats to liquefy and pass through rather than being removed by primary treatment
- Meat processing wastewater contains negligible amounts of either of these pollutants.

About 50% of the total phosphorus and sodium contaminants are generated from manure and paunch wastes, which come from stockyard washing, emptying of the animal stomachs and further processing of internal organs. Wastewater from these processes is often combined and referred to as the “green” stream, and is primary treated separately from the “red” stream. This “red” waste stream is generated mainly from water used to guarantee modern hygienic practice in the facility, and which becomes contaminated with blood and fats. Blood is the main source of nitrogen followed by urine and proteins from meat scraps. Blood recovery should be maximised and water entering blood containment areas should be avoided.

Rendering, often called the ‘by-products department’, and incorporating blood processing, is responsible for about 60% of COD and 20–40% of the sodium, phosphorus and nitrogen liberated to the wastewater. The major sources of nitrogen, phosphorus and sodium include the raw materials bin drainage and blood processing, whereas COD is primarily sourced from tallow refining. Smaller facilities may not operate a rendering plant. Waste streams from these operations may also be included in “red” streams.

### III. WASTE MINIMISATION STRATEGIES

Minimising waste into the water stream will reduce the wastewater load to the treatment system. This source reduction will have a direct impact on the costs associated with water usage.

It is very important that storm water be divided from wastewater streams to the maximum extent possible in order to reduce volumes.

Effluent disposal objectives depend on the disposal route and the surrounding environment. For each disposal route, the effluent must meet the required regulatory disposal standard. These may vary from state to state and are dependent on local and state legislations. The correct effluent disposal criteria should be obtained from the relevant regulatory authority. The legislation of Albania (No. 177) is given in the Table 1:

**TABLE 1**  
**LEGISLATION FOR MEAT AND MEAT BY-PRODUCT WASTEWATERS DISCHARGES**

Parameters	Normal values from the legislation
pH	6-9
Suspended Solid	50 mg/l
BOD <sub>5</sub>	50 mg/l
COD	250 mg/l
Vegetable oil	10 mg/l
Nitrogen	10 mg/l
Phosphorus	5 mg/l

Effluent disposal via sewer is best suited to generally larger abattoirs located close to residents. Best practice wastewater treatment will generally consist of:

- Oil and grease removal,
- Suspended solids and BOD reduction,
- Nitrogen and phosphorus reduction,
- Monitoring and reporting to the authority.

#### IV. MATERIAL AND METHODS

The raw wastewater was collected from meat and meat by product industry in Tirana, Albania.

For the pretreatment studies was used inorganic coagulant like ferric chloride. Ferric chloride was taken from “National Environmental Agency” in Albania. Activated sludge was taken from the impiant of wastewater treatment in Durres. The first sampe of activated slugde was taken from oxygenation area and the second from the second settler.

Wastewater sample collected from meat industry was filtered and the filtered water samples were then subjected to coagulant and AS treatment.

##### a. Optimization of the coagulant and activated sludge dosages:

The dosages were varied from 100 to 1000 mg/L. The addition of coagulant was followed by stirring for 5 min on magnetic stirrer and settling for 120 min and the same for theactivated sludge.

##### b. Optimization of pH for an individual coagulant:

pHs selected were 4.0, 6.5 and 9.0. pH of the wastewater was maintained with the help of 1:1 HCl and 0.1N NaOH, whenever required.

##### c. Optimization of settling time after coagulation:

The settling time intervals were varied between 30–120 min to get the best possible results.

The laboratory procedures are: Dissolved oxygen according to S SH EN 25714-2003, COD according to ISO15705-2002, BOD<sub>5</sub> according to ISO 7393-1, ISO 6107, P-PO<sub>4</sub> (with ascorbic acid), N-NH<sub>4</sub> according to ISO 7150:1984.

Coagulation–flocculation is one of the most important physicochemical treatment steps in industrial wastewater treatment to reduce the suspended and colloidal materials responsible for turbidity of the wastewater and also for the reduction of organic matters which contributes to the high level of BOD and COD content of the wastewater. In Table 3,<sup>(1),(2)</sup>are index for the treatment with AS respectively <sup>(1)</sup>for the AS from the oxygenation area and <sup>(2)</sup>AS in the second settler.

**TABLE 2**  
**RESULTS BEFORE TREATMENT OF WASTE WATER DISCHARGE**

Parameters	Values
pH	7.25
Temperature	22.5 °C
TDS	1825 mg/l
Konductivity	3650 µs/cm
N-NH <sub>4</sub>	30.1 mg /l
COD	3928 mg O/l
BOD <sub>5</sub>	2200 mg O/l
N-NO <sub>2</sub>	5.42 mg /l
N-NO <sub>3</sub>	8.28 mg /l
P-PO <sub>4</sub>	38.4 mg /l
P-tot	49.1 mg /l
SS	475 mg/l
Oil & Grease	775 mg/l
Alcalinity	18.9 milimol/l



**TABLE 3**  
**RESULTS AFTER TREATMENT WITH COAGULANT AND ACTIVATED SLUDGE OF WASTE WATER DISCHARGE**

Parameters	Before treatment values	After treatment values	Normal values
TDS	1825 mg O/l	650 mg/l <sup>(1)</sup>	-
TDS		645 mg/l <sup>(2)</sup>	-
COD	3928 mg O/l	1252 mg O/l <sup>(1)</sup>	250
COD		928 mg O/l <sup>(2)</sup>	250
BOD <sub>5</sub>	2200 mg O/l	162 mg O/l <sup>(2)</sup>	50
N-NO <sub>2</sub>	5.42 mg O/l	1.012 mg/l <sup>(1)</sup>	-
N-NO <sub>2</sub>		1.004 mg/l <sup>(2)</sup>	-
N-NO <sub>3</sub>	8.28 mg /l	0.071 mg/l <sup>(2)</sup>	-
N-NH <sub>4</sub>	30.1 mg /l	2.03 mg/l <sup>(2)</sup>	-
P-PO <sub>4</sub>	38.4 mg O/l	3.76 mg/l <sup>(1)</sup>	-
P-PO <sub>4</sub>		8.27 mg/l <sup>(2)</sup>	-
P-tot	49.1	8.6 mg /l <sup>(2)</sup>	5
SS	475 mg/l	213 mg/l <sup>(1)</sup>	50
SS		186 mg/l <sup>(2)</sup>	50
pH	7.25	7.53 <sup>(2)</sup>	6-9

## V. CONCLUSION

From the analysis of the physical-chemical indicators in the polluted waters discharged by the meat processing industry, all the parameters set were at a very high rate, in contradiction with the parameters set by the Albanian legislation on the Pollution Rate in the waters discharged by this industry. Treatment with the active sludge obtained from the secondary decanter resulted in a higher reduction of all the parameters.

The percentage reduction of the parameters from the treatment with AS from second settler are: TDS 64.66%; SS 60.84%; COD 76.37%; BOD<sub>5</sub> 92.64%; N-NO<sub>2</sub> 81.48%; N-NO<sub>3</sub> 99.14%, N-NH<sub>4</sub> 93.21%; P-PO<sub>4</sub> 90.21% and P-Tot 82.48%.

To prevent pollution, industries should stop immediately discharge wastewater in high values and to use methods or treatment that increase the efficiency of the removal of the organic matter in wastewater.

From this study we recommend that the meat industries should remove the solid mass (fat) to avoid the difficulty of the filtration process and treating wastewater with coagulant and active sludge to realize the reduction of parameters.

Design an anaerobic treatment process for wastewater treatment in slaughterhouses, as a high rate of COD reduction at a lower cost than aerobic systems is achieved and gas-generating methane-rich gas can be used as fuel.

## REFERENCES

- [1] Brett, S., Guy, J., Morse, GK. 1997. *Phosphorus Removal and Recovery Technologies*. Selper Publications, London.
- [2] Cooper, RN., Russell, JM. (1991). *Meat industry processing waste: characteristics and treatment*. Ency. Food Sci. and Tech. John Wiley, New York.
- [3] Cooper, RN., Russell, JM., Adam, JL. 1982b. *Recovery and utilization of protein from slaughterhouse effluents by chemical precipitation*. Upgrading Wastes for Feeds and Food, Butterworths, London.
- [4] Stephenson, P. (1978). *A method of physico-chemical treatment of organic wastewaters*. Proc. of the 9th EPA Nat. Sym. of Food Processing Wastes, Denver, Colorado.
- [5] McGrath, JW, Quinn, JP. (2004). *Biological phosphorus removal in Phosphorus in Environmental Technologies – Principles and Applications*. Valsami-Jones, E (ed). Integrated Environmental Technology Series. IWA Publishing, London.
- [6] Andrews, J. F., and S.P. Graef, 1970. Dynamic Modeling and Simulation of the Anaerobic Digestion Process. *Advances in Chemistry*
- [7] Joint Task Force of the Water Environment Federation and the American Society of Civil Engineers, 1992. *Design of Municipal Wastewater Treatment Plants Volume II*.
- [8] EU Commission Sept. 2003 *Draft Reference Document on Best Available Techniques in the Slaughterhouses and Animal By-products Industries*, Seville.



**AD Publications**

**Sector-3, MP Nagar, Bikaner,  
Rajasthan, India**

**[www.adpublications.org](http://www.adpublications.org), [info@adpublications.org](mailto:info@adpublications.org)**